



1 **Drivers of biogenic secondary organic aerosol from the past to the future**

2 Yang Shi^{1,2}, Colette L. Heald³, Jesse H. Kroll¹

3 ¹Civil and Environmental Engineering Department, Massachusetts Institute of Technology,
4 Cambridge, MA 02139, USA

5 ²Atmospheric, Climate, and Earth Sciences Division, Pacific Northwest National Laboratory,
6 Richland, WA, USA

7 ³Institute for Atmospheric and Climate Science, ETH Zurich, Zurich, 8092, Switzerland

8

9 *Correspondence to:* Yang Shi (yang.shi@pnnl.gov) and Colette Heald
10 (colette.heald@env.ethz.ch)

11



12 **Abstract.**

13 Biogenic secondary organic aerosol (SOA) makes up a substantial fraction of atmospheric fine
14 particulate mass, with important implications for climate and human health. However, its
15 chemical formation processes remain poorly understood and are often oversimplified in 3D
16 atmospheric models. Recent studies have found that the peroxy radical (RO_2) isomerization and
17 the RO_2 accretion reactions ($RO_2 + RO_2$) can lead to SOA formation. We expand the RO_2
18 chemical mechanism in the Community Earth System Model version 2 to include these two
19 additional pathways for biogenic SOA formed through the OH oxidation of volatile organic
20 compounds (VOCs). Using this mechanism, we quantify the contribution of each RO_2 pathway
21 to biogenic SOA formation and examine how these contributions evolve from the pre-industrial
22 (PI) to present-day (PD) and future (F). We find that in PD conditions, RO_2 isomerization
23 accounts for 44-46% of monoterpene SOA, while the contribution from $RO_2 + RO_2$ pathways is
24 minor. From PI to F, the RO_2 fate varies in response to atmospheric NO_x levels and climate, but
25 the contribution from RO_2 isomerization is consistently high for monoterpenes, underscoring the
26 importance of representing this pathway in SOA parameterizations. In addition, total biogenic
27 SOA formed through OH oxidation decreases by 41% from PI to PD and increases by 113%
28 from PD to F, driven primarily by changes in biogenic VOC emissions. Our results highlight the
29 need to better constrain RO_2 pathways for SOA formation through laboratory studies and
30 represent this RO_2 chemistry in SOA modeling.

31



32 **Short summary**

33 We implement secondary organic aerosol (SOA) formation pathways due to peroxy radical (RO₂)
34 isomerization and accretion reactions in the CESM2 model. The contribution of RO₂ pathways to
35 SOA formation varies from the past to the future; for monoterpenes RO₂, isomerization remains
36 important under all climate conditions. We also quantify changes in total biogenic SOA burden
37 under different climates. Our study highlights the need to better represent RO₂ chemistry in SOA
38 modeling.

39



40 **1 Introduction**

41 Aerosols impact the Earth's climate by directly scattering and absorbing radiation as well
42 as indirectly altering cloud properties (Forster et al., 2021). They also contribute to air pollution
43 and the associated harm to human health (Burnett et al., 2018). Organic aerosol (OA) makes up a
44 substantial fraction (20-90%) of submicron particulate mass in the troposphere, with formation
45 of secondary organic aerosol (SOA) generally outweighing primary OA (Jimenez et al., 2009;
46 Zhang et al., 2007). Biogenic sources are estimated to be a major contributor to global SOA
47 formation (Hallquist et al., 2009; Hodzic et al., 2016; Kanakidou et al., 2005; Tilmes et al.,
48 2019). Despite this, there remain large uncertainties in our understanding of biogenic SOA,
49 largely due to the complex chemical processes involved in the formation of SOA.

50 SOA is formed through the oxidation of volatile organic compounds (VOCs) followed by
51 gas-to-particle conversion of the products. VOC oxidation generates organic peroxy radicals
52 (RO_2), the chemical fate of which is a determining factor in SOA formation. Historically,
53 chamber studies explored SOA formation when RO_2 reacts with NO under high- NO_x (polluted)
54 conditions and with HO_2 under low- NO_x (clean) conditions (Kroll et al., 2005, 2006; Ng et al.,
55 2007; Song et al., 2005). For small biogenic VOC (BVOC) molecules (e.g., isoprene and
56 monoterpenes), the SOA yields (i.e., the mass of SOA formed per mass of VOC reacted) are
57 generally larger for the $\text{RO}_2 + \text{HO}_2$ pathway than the $\text{RO}_2 + \text{NO}$ pathway, because the products
58 formed from the former reaction are less volatile (Kroll et al., 2006; Presto et al., 2005). But this
59 NO_x dependence is reversed in the oxidation of large VOC molecules (e.g., sesquiterpenes) (Ng
60 et al., 2007).

61 Recent studies have elucidated additional RO_2 reaction pathways for SOA formation.
62 Chamber experiments on α -pinene oxidation have shown that RO_2 unimolecular isomerization,



63 also known as autooxidation, generates large amounts of extremely low-volatility products that
64 can easily condense to form SOA (Ehn et al., 2014). The reaction rates of isomerization highly
65 depend on the chemical structures of RO₂ (Bianchi et al., 2019; Vereecken and Nozière, 2020;
66 Otkjær et al., 2018; Borcher et al., 2026). For some RO₂ species, the isomerization is sufficiently
67 fast and can outcompete bimolecular reactions (L. Xu et al., 2019; R. Xu et al., 2022). Also,
68 isomerization rates exhibit a large positive temperature dependence, enhancing the relative
69 importance of this pathway at higher temperatures (Bianchi et al., 2019). In addition, chamber
70 experiments with α -pinene and aromatic compounds have revealed that RO₂ self- and cross-
71 reactions (i.e., RO₂ + RO₂ reactions) can rapidly form accretion (dimer) products, which feature
72 remarkably low volatility and are thus effective sources for SOA (Berndt et al., 2018a, b; Zhao et
73 al., 2018). The reaction rates of the RO₂ + RO₂ reactions are highly uncertain, with measured
74 rates varying by up to 2 orders of magnitude in these chamber studies.

75 VOC oxidation and the subsequent RO₂ chemistry are often simplified in SOA
76 parameterizations in regional and global models. In earlier models lacking comprehensive
77 chemical mechanisms, emissions of SOA or gas-phase condensable organic products were scaled
78 directly from VOC emissions with fixed mass yields (Chin et al., 2002; Colarco et al., 2010; Liu
79 et al., 2012). A more advanced approach is to oxidize VOC into two or more condensable
80 product bins (Bergman et al., 2022; Chung and Seinfeld, 2002; Hoyle et al., 2007; Lou et al.,
81 2020; Tilmes et al., 2019; Tsimpidi et al., 2014). However, this method does not account for the
82 NO_x dependence of the RO₂ fate, and some models use only the low-NO_x conditions for biogenic
83 SOA, assuming that most biogenic emissions are oxidized in relatively clean environments (e.g.,
84 Lou et al., 2020; Tilmes et al., 2019; Tsimpidi et al., 2014). The first explicit treatment of NO_x-
85 dependent RO₂ chemistry was introduced by Henze et al. (2008), who parameterized aromatic



86 SOA yields from both the low-NO_x and high-NO_x pathways as products of the RO₂ + HO₂ and
87 RO₂ + NO reactions, respectively. Some large-scale models have adopted this approach for both
88 anthropogenic and biogenic SOA (Hodzic et al., 2016; Jo et al., 2021; Pye et al., 2010). More
89 recently, a few attempts have been made to include the isomerization and RO₂ + RO₂ reaction
90 pathways with more comprehensive RO₂ chemistry in large scale models (Mayhew et al., 2025;
91 R. Xu et al., 2022; Zhao et al., 2020, 2024). R. Xu et al. (2022) represent the two pathways for
92 RO₂ generated from isoprene and monoterpene OH reactions and ozonolysis in a chemical
93 transport model. However, they do not couple the gas-phase chemistry with aerosol formation
94 and use the formed low-volatility gas-phase products as an analogue for SOA. Mayhew et al.
95 (2025) examined the accretion reactions for all the RO₂ generated in the same chemical transport
96 model, but the isomerization of terpene RO₂ is precluded. Zhao et al. (2020) developed an RO₂-
97 pathway (including autooxidation and dimerization) SOA formation scheme for monoterpenes,
98 which they implement in a regional model over the Amazon. This scheme was subsequently
99 implemented in a global climate model to better simulate organic-mediated nucleation (Zhao et
100 al., 2024). To our knowledge, the impact of these two newly identified RO₂ fates on total
101 biogenic SOA formation has not yet been explored in a global model.

102 The RO₂ fate and biogenic SOA formation under different climate conditions are
103 controlled by complex interactions between natural biogenic VOC emissions, anthropogenic
104 emissions, and climate factors (e.g., temperature, CO₂ concentrations). For example, global
105 biogenic VOC emissions are influenced by anthropogenic land use change (Heald and Geddes,
106 2016; Shi et al., 2025; Unger, 2014), temperatures (Guenther et al., 2012), and CO₂ level (Armeth
107 et al., 2007; Heald et al., 2009). Changes in anthropogenic NO emissions may perturb the RO₂ +
108 NO pathway and thus shift the RO₂ fate and SOA formation (Jo et al., 2021). Also, global



109 warming from the past to the future may lead to opposing effects – increasing SOA formation
110 through accelerating RO₂ isomerization while reducing SOA by pushing gas-particle partitioning
111 toward the gas-phase. The role of these factors on biogenic SOA formation remains poorly
112 constrained, partly due to a lack of representation of comprehensive RO₂ chemistry in the SOA
113 parameterizations in global climate models. As a result, the SOA loadings under different
114 climate conditions are not well assessed, which imposes large uncertainties in the aerosol-
115 induced climate radiative forcing and potential climate feedback involving biogenic SOA.

116 In this study, we incorporate the latest understanding of RO₂ chemistry for biogenic SOA
117 initially formed from gas-phase OH-initiated oxidation in a global climate model. We focus on
118 the fate of the initial RO₂ formed upon VOC oxidation. We note that SOA can also form through
119 VOC reaction with other oxidants (e.g., O₃ and NO₃) and through multiphase chemistry.
120 Although these pathways also involve RO₂ chemistry, their specific RO₂ fates are not the
121 primary focus of this study and thus they are excluded from our analysis. Our work aims to
122 answer three questions: (1) How does our recent understanding of RO₂ fate alter the global
123 simulated burden of OH-initiated biogenic SOA?; (2) What fraction of RO₂ undergoes each
124 reaction pathway (i.e., RO₂ fate) and how much SOA is formed through each pathway?; and (3)
125 How does the burden of SOA and RO₂ fate change from the past to the present and to the future?

126 **2 Methods**

127 **2.1 CESM2.2**

128 Our study uses the Community Earth System Model version 2.2 (CESM2.2; Danabasoglu
129 et al., 2020). The atmosphere component of CESM2.2 is the Community Atmosphere Model
130 version 6 with full chemistry (CAM6-Chem; Emmons et al., 2020). CAM6-Chem incorporates



131 the MOZART-TS2 gas-phase chemistry (Model of Ozone And Related chemical Tracers;
132 Schwantes et al., 2020) with the volatility basis set (VBS) scheme for SOA formation (Tilmes et
133 al., 2019). The VBS scheme considers the OH, O₃, and NO₃ gas-phase oxidation of six BVOC
134 species, including isoprene (ISOP), four monoterpenes (MTERP) – α -pinene (APIN), β -pinene
135 (BPIN), limonene (LIMON), and myrcene (MYRC) – and one lumped sesquiterpene, beta-
136 caryophyllene (BCARY). The OH-oxidation accounts for the high-NO_x (RO₂ + NO) and low-
137 NO_x (RO₂ + HO₂) conditions (Hodzic et al., 2016; Jo et al., 2021) (Table 1). The VBS reactions
138 produce semi-volatile SOA precursor gases (SOAG) into five logarithmically spaced bins based
139 on their saturation concentration (C^{*}). These bins have C^{*} of 0.01, 0.1, 1, 10, and 100 $\mu\text{g}/\text{m}^3$ at
140 300 K and are designated as SOAG0, SOAG1, SOAG2, SOAG3, SOAG4 in the model,
141 respectively. The SOAGs undergo gas-aerosol partitioning and form SOA in the Aitken and
142 accumulation modes of the 4-mode version of the Modal Aerosol Model (MAM4; [Liu et al.,](#)
143 [2016](#)). SOA is subject to photolysis loss at a constant rate of 0.04% of J_{NO_2} (Hodzic et al., 2015).
144 The MOZART-TS2 gas phase mechanism includes a more comprehensive BVOC gas-phase
145 oxidation than is treated in the default VBS scheme. In addition to the reactions of RO₂s with
146 HO₂ and NO, its OH-oxidation mechanism includes the reactions of terpene RO₂s with NO₃,
147 CH₃O₂, CH₃CO₃, and selected RO₂ species, as well as reactions of ISOP RO₂s with CH₃O₂ and
148 CH₃CO₃, along with the isomerization and dissociation of ISOP RO₂s. These additional RO₂ loss
149 pathways are not connected to SOA simulation. Also, the MOZART-TS2 reactions do not form
150 SOAG.



151 **Table 1.** BVOC OH oxidation and RO₂ reactions in default CAM6-Chem VBS. For simplicity in
 152 this table, we use MTERP to represent the four monoterpenes in CAM6-Chem (APIN, BPIN,
 153 LIMON, and MYRC). ISOPO2VBS (C₅H₉O₃), MTERPO2VBS (C₁₀H₁₇O₃), and
 154 BCARYO2VBS (C₁₅H₂₅O₃) are first-generation peroxy radicals formed from isoprene (ISOP),
 155 monoterpene (MTERP), and sesquiterpene (BCARY) oxidation in VBS, respectively. Chemical
 156 formula for other species can be found in Table S2 of Schwantes et al. (2020).

Reactions	Rate (cm ³ molecule ⁻¹ s ⁻¹)
ISOP + OH → ISOP + OH + ISOPO2VBS	$2.7 \times 10^{-11} \times e^{(390/T)}$
ISOPO2VBS + HO ₂ → HO ₂ + 0.0031*SOAG0 + 0.0035*SOAG1 + 0.0003*SOAG2 + 0.0271*SOAG3 + 0.0474*SOAG4	$2.12 \times 10^{-13} \times e^{(1300/T)}$
ISOPO2VBS + NO → NO + 0.0003*SOAG0 + 0.0003*SOAG1 + 0.0073*SOAG2 + 0.0057*SOAG3 + 0.0623*SOAG4	$2.7 \times 10^{-12} \times e^{(360/T)}$
MTERP + OH → MTERP + OH + MTERPO2VBS	See note*
MTERPO2VBS + HO ₂ → HO ₂ + 0.0508*SOAG0 + 0.1149*SOAG1 + 0.0348*SOAG2 + 0.0554*SOAG3 + 0.1278*SOAG4	$2.6 \times 10^{-13} \times e^{(1300/T)}$
MTERPO2VBS + NO → NO + 0.0245*SOAG0 + 0.0082*SOAG1 + 0.0772*SOAG2 + 0.0332*SOAG3 + 0.13*SOAG4	$2.7 \times 10^{-12} \times e^{(360/T)}$
BCARY + OH → BCARY + OH + BCARYO2VBS	2×10^{-10}
BCARYO2VBS + HO ₂ → HO ₂ + 0.2202*SOAG0 + 0.2067*SOAG1 + 0.0653*SOAG2 + 0.1284*SOAG3 + 0.114*SOAG4	$2.75 \times 10^{-13} \times e^{(1300/T)}$
BCARYO2VBS + NO → NO + 0.1279*SOAG0 + 0.1792*SOAG1 + 0.0676*SOAG2 + 0.079*SOAG3 + 0.1254*SOAG4	$2.7 \times 10^{-12} \times e^{(360/T)}$

157 *The reaction rates for the OH oxidation of APIN, BPIN, LIMON, and MYRC are
 158 $1.34 \times 10^{-11} \times e^{(410/T)}$, $1.62 \times 10^{-11} \times e^{(460/T)}$, $3.41 \times 10^{-11} \times e^{(470/T)}$, and 2.1×10^{-10}
 159 cm³ molecule⁻¹ s⁻¹, respectively.

160 CAM6-Chem is coupled with the land component of CESM2 – the Community Land
 161 Model version 5 (CLM5, Lawrence et al., 2019). The model is run with the satellite phenology
 162 biogeochemistry configuration, where the land use and leaf area index are prescribed and not
 163 impacted by changes in CO₂ and climate. CLM5 includes the Model of Emissions of Gases and
 164 Aerosols from Nature (MEGAN) version 2.1 (Guenther et al., 2012), which prognostically



165 calculates BVOC emissions accounting for light, temperature, leaf age, and CO₂. In MEGAN,
166 ISOP emissions are inhibited by elevated CO₂ level (Heald et al., 2009), while this effect does
167 not influence MTERP and BCARY emissions.

168 **2.2 Expanded RO₂ chemistry**

169 To improve the representation of biogenic SOA formation, we expand the RO₂ chemistry
170 in the VBS scheme. As mentioned above, we focus on the RO₂ reactions related to OH-initiated
171 biogenic SOA formation, which represents 59% of total biogenic SOA in the baseline CAM6-
172 chem under PD climate conditions (estimated from the BASE experiment as described in Section
173 2.4). Hereafter, the RO₂ reactions and the formed SOA exclusively refer to those initiating from
174 BVOC + OH reactions. We note that our mechanism focuses on gas-phase reactions, whereas the
175 SOA formation through heterogeneous chemistry is not considered. Also, we only represent the
176 fate of the first generation RO₂, though later generation RO₂ are included in the RO₂ + RO₂
177 reactions (see below for more details). The RO₂ formed from the four MTERPs are lumped
178 together in the modified VBS and assumed to have the same yields and reaction rates for the RO₂
179 reactions.

180 Our modifications primarily focus on incorporating isomerization and RO₂ + RO₂
181 reactions for the first-generation terpene RO₂ (MTERP-RO₂ and BCARY-RO₂) (Table 2).
182 Following Pye et al. (2019), we allow 22% of the formed MTERP-RO₂ to undergo isomerization
183 and with a 50% yield to the lowest volatility bin of SOA (SOAG0) (Table 2, part 1). This is
184 implemented by partitioning the total MTERP-RO₂ into two species (0.78 and 0.22 fractions)
185 that undergo identical chemistry, except that only the latter is allowed to isomerize. The
186 temperature-dependent isomerization reaction rate was estimated using a rate constant of 0.28 s⁻¹
187 at 293K (Pye et al., 2019) and an activation energy barrier of 18 kcal/mol (Bianchi et al., 2019).



188 It is important to note that the branching ratio, SOA yields, and reaction rates are subjected to
189 significant uncertainties. For example, the isomerization rate used in this study may lie at the
190 lower end – Xu et al. (2019) reported unimolecular rate constants of 4 ± 2 and $16 \pm 5 \text{ s}^{-1}$ at 296 K
191 for α -pinene and β -pinene, respectively. Nevertheless, even with these slower rates,
192 isomerization remains relatively fast compared with competing bimolecular reactions, especially
193 under clean and/or warm conditions (Figure 1). The fast rate, along with the high SOAG yields,
194 leads to rapid production of large amounts of SOA from isomerization. Also, isomerization is
195 highly temperature-dependent as compared to the bimolecular reactions (Figure 1).
196



197 **Table 2.** Newly implemented reactions for MTERP-RO₂ (MTERPO2VBS) and BCARY-RO₂
 198 (BCARYO2VBS) in VBS. Units for isomerization reaction rate constants are s⁻¹ and those for
 199 the RO₂ + RO₂ reactions and other terpene RO₂ reactions are cm³ molecule⁻¹ s⁻¹.

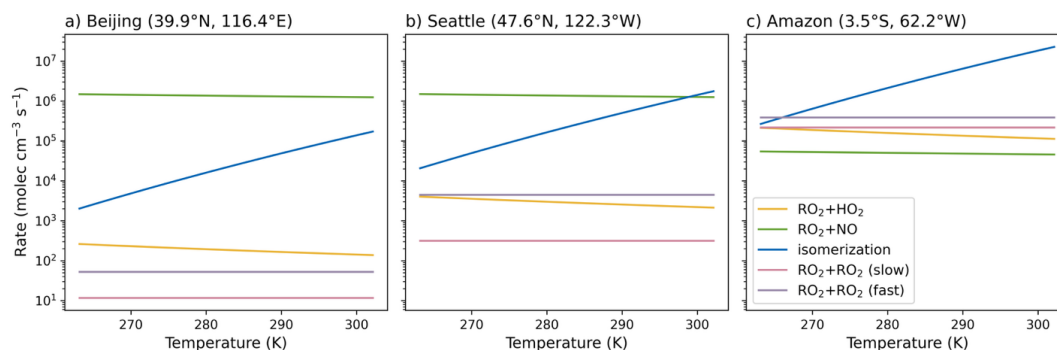
Reactions	Reaction rate constant		References
Part 1. Isomerization*			
MTERPO2VBS → 0.5SOAG0 [a]	$7.48 \times 10^{12} e^{(-9058/T)}$ [a, b]		[a] Pye et al. (2019); [b] Bianchi et al. (2019)
BCARYO2VBS → 0.5SOAG0 [a]	$7.48 \times 10^{12} e^{(-9058/T)}$ [a, b]		
Part 2. RO₂ + RO₂ reactions			
	Fast	Slow	
MTERPO2VBS + ISOP-RO ₂ [†] → 0.04SOAG0 [c]	2×10^{-11} [d]	2×10^{-11} [d]	[c] Zhao et al. (2018); [d] Berndt et al. (2018b); [e] Berndt et al. (2018a)
MTERPO2VBS + IEPOXOO → 0.04SOAG0 [c]	2×10^{-11} [d]	2×10^{-11} [d]	
MTERPO2VBS + MTERPO2VBS → 0.04SOAG0 [c]	4×10^{-11} [d]	10^{-12} [c]	
MTERPO2VBS + BCARYO2VBS → 0.04SOAG0 [c]	4×10^{-11} [d]	10^{-12} [c]	
MTERPO2VBS + TP2-RO ₂ [‡] → 0.04SOAG0 [c]	2.6×10^{-10} [e]	10^{-12} [c]	
BCARYO2VBS + ISOP-RO ₂ → 0.04SOAG0 [c]	2×10^{-11} [d]	2×10^{-11} [d]	
BCARYO2VBS + IEPOXOO → 0.04SOAG0 [c]	2×10^{-11} [d]	2×10^{-11} [d]	
BCARYO2VBS + BCARYO2VBS → 0.04SOAG0 [c]	4×10^{-11} [d]	10^{-12} [c]	
BCARYO2VBS + TP2-RO ₂ → 0.04SOAG0 [c]	2.6×10^{-10} [e]	10^{-12} [c]	
Part 3. Other terpene RO₂ reactions that are newly added to VBS but do not form SOAG			
MTERPO2VBS + NO ₃ → NO ₃	2.3×10^{-12}		Schwantes et al. (2020)
MTERPO2VBS + CH ₃ O ₂ → CH ₃ O ₂	2×10^{-12}		
MTERPO2VBS + CH ₃ CO ₃ → CH ₃ CO ₃	$2 \times 10^{-12} \times e^{(500/T)}$		
BCARYO2VBS + NO ₃ → NO ₃	2.3×10^{-12}		
BCARYO2VBS + CH ₃ O ₂ → CH ₃ O ₂	2×10^{-12}		
BCARYO2VBS + CH ₃ CO ₃ → CH ₃ CO ₃	$2 \times 10^{-12} \times e^{(500/T)}$		

200 *Only 22% of MTERPO2VBS can isomerize (Pye et al., 2019).

201 [†]ISOP-RO₂ denotes six first generation ISOP-RO₂ species from MOZART-TS2, including
 202 ISOPED1O₂, ISOPB1O₂, ISOPZD1O₂, ISOPED4O₂, ISOPB4O₂, and ISOPZD4O₂.

203 [‡]TP2-RO₂ denotes RO₂ formed through terpenes ozonolysis and those from the second and later
 204 generation oxidation in MOZART-TS2, including TERP1OOHO₂, TERP2OOHO₂,
 205 TERPA1O₂, TERPA2CO₃, TERPA2O₂, TERPA3CO₃, TERPA3O₂, TERPA4O₂, TERPACO₃,
 206 TERPF1O₂, and TERPF2O₂.

207



208
 209 **Figure 1.** Loss rates for various MTERP-RO₂ reactions as a function of temperature at a)
 210 Beijing, b) Seattle, and c) Amazon. The rates are calculated based on reactant concentrations in
 211 June from the NEW_slow experiment, except for the fast RO₂ + RO₂ reactions, which use results
 212 from the NEW_fast experiment.

213 Next, we introduce RO₂ + RO₂ for MTERP-RO₂, considering the reactions with first-
 214 generation ISOP-RO₂, IEPOXOO, first-generation MTERP-RO₂ and BCARY-RO₂, the terpene
 215 RO₂ formed through terpene ozonolysis and the second or later generation oxidation (Table 2,
 216 part 2). These reactants are produced in MOZART-TS2. The reactions with nitrogen-containing
 217 biogenic RO₂ and RO₂ formed from the oxidation of other organics are not included. We note
 218 that for the same set of reactions, the rate coefficients reported by different laboratory studies
 219 vary by up to two orders of magnitude (Berndt et al., 2018a, b; Zhao et al., 2018), highlighting
 220 the substantial uncertainty associated with these reactions rates. Therefore, following Xu et al.
 221 (2022), we classified and tested the RO₂ + RO₂ reaction rates as either fast or slow combinations.
 222 Moreover, the SOA yields of the RO₂ + RO₂ reactions are another source of uncertainty. All of
 223 the reactions are assumed to form 4% of SOAG₀, representing the lower limit of the dimer
 224 formation branching ratio reported by Zhao et al. (2018). For BCARY-RO₂, we add these two
 225 reaction pathways assuming they have the same behavior as MTERP-RO₂, due to the limited
 226 understanding of BCARY-RO₂ chemistry (Table 2). This assumption may result in an
 227 underprediction of BCARY SOA, since accretion reactions involving BCARY oxidation have



228 been found to generate products with lower volatility than those with monoterpene and isoprene
229 alone (Dada et al., 2023). Moreover, to examine the RO₂ fate and contribution to SOA formation
230 from each reaction, we track SOA formed from individual BVOC reactions separately in our
231 experiments. SOA formed through MTERP-RO₂ + ISOP-RO₂/BCARY-RO₂ are classified as
232 MTERP SOA, whereas those formed through the cross reaction between ISOP-RO₂ and
233 BCARY-RO₂ are classified as BCARY SOA.

234 Finally, we characterize the fates of the RO₂ that are included in the MOZART chemistry
235 but do not form SOA in the VBS. For terpene RO₂, we implement their reactions with NO₃,
236 CH₃O₂, and CH₃CO₃ in the VBS (Table 2, part 3). For ISOP-RO₂, instead of generating a new
237 RO₂ species (i.e., ISOP₂VBS in Table 1), we directly use the six ISOP-RO₂ (ISOPED1O₂,
238 ISOPB1O₂, ISOPZD1O₂, ISOPED4O₂, ISOPB4O₂, and ISOPZD4O₂) formed from the
239 MOZART chemistry in the RO₂ + HO₂ and RO₂ + NO reactions in VBS (i.e., replace the ISOP
240 reactions in Table 1 with those in Table 3, part 1). In this way, the VBS and MOZART are
241 coupled for ISOP-RO₂, and additional key ISOP-RO₂ reactions (isomerization, dissociation, and
242 reactions with CH₃O₂, and CH₃CO₃) (Table 3, part 2) are considered in the VBS. These reactions
243 do not form SOAG but represent additional loss pathways for RO₂ within the VBS, which would
244 reduce SOA formation via competition with the SOAG-producing reactions. In our mechanism,
245 we assume that ISOP-RO₂ isomerization does not form SOAG because the isomerization
246 products are volatile (D'Ambro et al., 2017). However, a recent study found that isomerization of
247 ISOP-RO₂ forms SOA with molar yields of 0.13-0.35% (Berndt et al., 2025), suggesting that the
248 global total isoprene SOA yields in our simulations may be a lower limit.

249



250 **Table 3.** ISOP-RO₂ reactions in the modified VBS and the related RO₂ fate in MOZART. Units
 251 for reaction rate constants are cm³ molecule⁻¹ s⁻¹, except for specific notations.

Reactions	Rate constant
Part 1. ISOP-RO₂ reactions in VBS	
ISOP-RO ₂ * + HO ₂ → ISOP-RO ₂ * + HO ₂ + 0.0031*SOAG0 + 0.0035*SOAG1 + 0.0003*SOAG2 + 0.0271*SOAG3 + 0.0474*SOAG4	$2.12 \times 10^{-13} \times e^{(1300/T)}$
ISOP-RO ₂ * + NO → ISOP-RO ₂ * + NO + 0.0003*SOAG0 + 0.0003*SOAG1 + 0.0073*SOAG2 + 0.0057*SOAG3 + 0.0623*SOAG4	$2.7 \times 10^{-12} \times e^{(360/T)}$
Part 2. Related ISOP-RO₂ fate in MOZART	
ISOPZD1O2 → 0.15*HPALDB1C + 0.25*HPALD1 + 0.4*HO2 + 0.6*OH + 0.6*DHPMPAL + 0.6*CO	$5.05 \times 10^{15} \times e^{(-12200/T)} \times e^{(10^8/T^3)\dagger}$
ISOPZD4O2 → 0.15*HPALDB4C + 0.25*HPALD4 + 0.4*HO2 + 0.6*OH + 0.6*DHPMPAL + 0.6*CO	$2.22 \times 10^9 \times e^{(-7160/T)} \times e^{(10^8/T^3)\dagger}$
ISOPB1O2 → MVK + CH2O + OH	$1.04 \times 10^{11} \times e^{(-9746/T)\dagger}$
ISOPB4O2 → MACR + CH2O + OH	$1.88 \times 10^{11} \times e^{(-9752/T)\dagger}$
ISOPED1O2 + CH3O2 → 0.25*CH3OH + 0.25*ISOPOH + 0.75*CH2O + 0.72*HO2 + 0.28*CO + 0.28*OH + 0.28*MVKOOH + 0.47*HYDRALD	1.2×10^{-12}
ISOPZD1O2 + CH3O2 → 0.25*CH3OH + 0.25*ISOPOH + 0.75*CH2O + 0.72*HO2 + 0.28*CO + 0.28*OH + 0.28*MVKOOH + 0.47*HYDRALD	
ISOPB4O2 + CH3O2 → 0.25*CH3OH + 0.25*HYDRALD + 0.25*ISOPOH + 1.25*CH2O + HO2 + 0.5*MACR	1.4×10^{-12}
ISOPZD4O2 + CH3O2 → 0.25*CH3OH + 0.25*ISOPOH + 0.75*CH2O + 0.72*HO2 + 0.28*CO + 0.28*OH + 0.28*MACROOH + 0.47*HYDRALD	9.8×10^{-13}
ISOPED4O2 + CH3O2 → 0.25*CH3OH + 0.25*ISOPOH + 0.75*CH2O + 0.72*HO2 + 0.28*CO + 0.28*OH + 0.28*MACROOH + 0.47*HYDRALD	
ISOPB1O2 + CH3O2 → 1.75*CH2O + 0.25*ISOPOH + 0.75*MVK + 1.5*HO2	1.6×10^{-13}
ISOPED1O2 + CH3CO3 → 0.45*HO2 + 0.45*HYDRALD + 0.55*CO + 0.55*OH + 0.55*MVKOOH + CO2 + CH3O2	$2 \times 10^{-12} \times e^{(500/T)}$
ISOPB1O2 + CH3CO3 → MVK + CH2O + HO2 + CO2 + CH3O2	
ISOPZD1O2 + CH3CO3 → 0.45*HO2 + 0.45*HYDRALD + 0.55*CO + 0.55*OH + 0.55*MVKOOH + CO2 + CH3O2	
ISOPED4O2 + CH3CO3 → 0.45*HO2 + 0.45*HYDRALD + 0.55*CO + 0.55*OH + 0.55*MACROOH + CO2 + CH3O2	
ISOPB4O2 + CH3CO3 → MACR + CH2O + HO2 + CO2 + CH3O2	
ISOPZD4O2 + CH3CO3 → 0.45*HO2 + 0.45*HYDRALD + 0.55*CO + 0.55*OH + 0.55*MACROOH + CO2 + CH3O2	

252 *ISOP-RO₂ denotes six first generation ISOP-RO₂ species from MOZART-TS2, including
 253 ISOPED1O2, ISOPB1O2, ISOPZD1O2, ISOPED4O2, ISOPB4O2, and ISOPZD4O2.

254 †Units: s⁻¹.



255 **2.3 Modifications to SOA photolysis**

256 Another source of uncertainty lies in the representation of SOA photolysis. The standard
257 CAM6-Chem assumes that all SOA is subject to photolysis at a constant rate. However,
258 laboratory studies have reported a photo-recalcitrant fraction ranging from 7% to 90% (O'Brien
259 and Kroll, 2019; Sun and Smith, 2024; Zawadowicz et al., 2020). Neglecting this fraction likely
260 results in an overestimation of SOA photochemical loss and thus an underprediction of SOA
261 mass in model simulations. Therefore, as a simple step to mimic the photo-recalcitrant fraction as
262 observed in laboratory studies, we turn off the photolysis of SOA in the lowest volatility bin.
263 This modification results in a mean photo-recalcitrant fraction of 29% in the modified
264 mechanism (calculated based on 1-year experiment using NEW_slow chemical mechanism; see
265 Section 2.4 for details about NEW_slow). We note that the SOA photolysis rate is also uncertain.
266 Some chamber experiments shows that the rate can reach as high as 2% of J_{NO_2} (Henry and
267 Donahue, 2012; Krapf et al., 2016), while recent laboratory studies reported rate of 0.025% J_{NO_2}
268 (Baboomian et al., 2020; Sun and Smith, 2024). Since the rate used in standard CAM6-Chem
269 (0.04% J_{NO_2}) is in general agreement with the more recent studies (Baboomian et al., 2020; Sun
270 and Smith, 2024), we leave the photolysis rate unchanged.

271 **2.4 Experiments**

272 We conduct three sets of experiments with CAM6-Chem. First, we compare the default
273 configuration with the modified RO₂ chemistry through three experiments: BASE, NEW_fast,
274 and NEW_slow. The BASE experiment represents the default chemical mechanism (with our
275 updates to the treatment of SOA photolysis), while NEW_fast and NEW_slow incorporate
276 modified RO₂ chemistry with fast and slow RO₂ + RO₂ reaction rates, respectively. These three



277 experiments utilize sea surface temperature (SST), CO₂ concentrations, anthropogenic and
278 natural emissions, and land use data from 2010, representing PD conditions. Second, we perform
279 two experiments – the PI and F experiments – with modified RO₂ chemistry that incorporates
280 slow RO₂ + RO₂ reaction rates under PI (1850) and F (2100) conditions (i.e., SST, CO₂
281 concentrations, anthropogenic and natural emissions, and land use). The future conditions follow
282 the Shared Socioeconomic Pathway 5-8.5 (hereafter SSP5), which assumes a fossil-based
283 economy with high CO₂ levels and projected temperature increase (Riahi et al., 2017). This is
284 also a strong pollution control scenario with reduced future anthropogenic emissions compared
285 to PD levels. By comparing PI and F with the NEW_slow (PD) experiment, we investigate how
286 the RO₂ fate and SOA formation change from the past to present and future. Finally, to isolate
287 the chemistry impacts, we conduct two additional experiments that are the same as PI and F,
288 except with fixed BVOC emissions at PD level (i.e., PI_PDB and F_PDB). All experiments are
289 performed with a horizontal resolution of 0.9° × 1.25° and 32 vertical layers. The model is
290 integrated for 11 years with the first year used for spin-up. Results are shown as 10-year
291 averages to minimize interannual climate variability.

292 **3 Results**

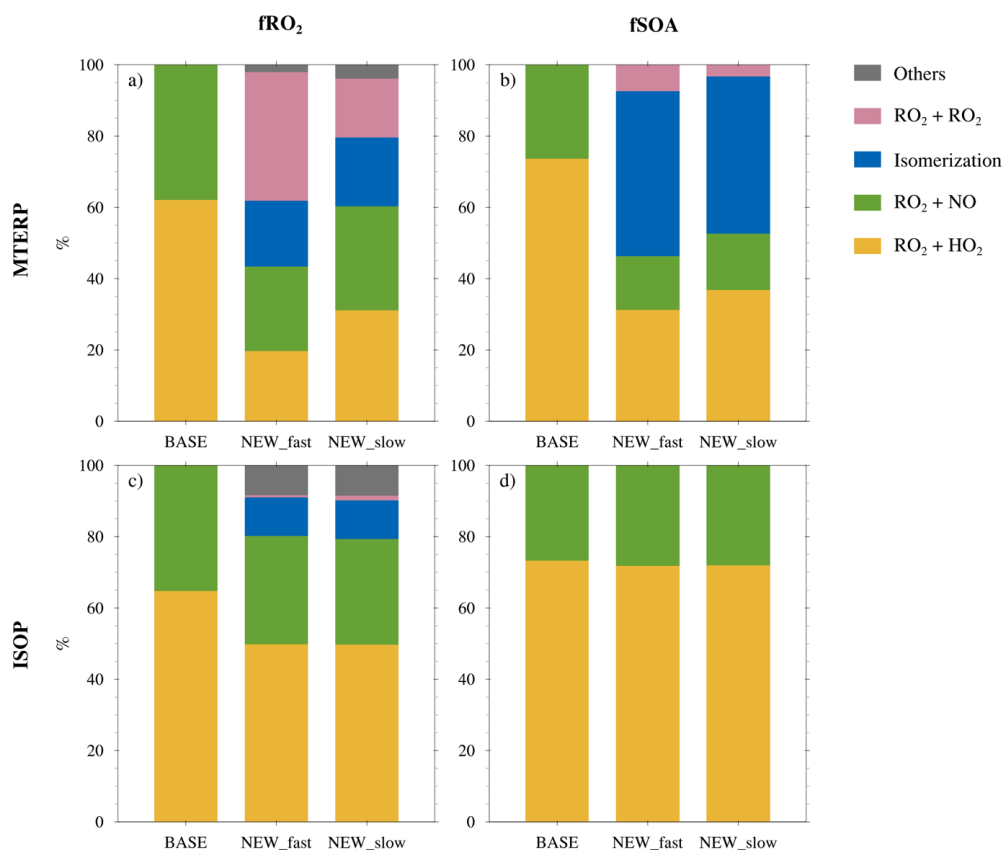
293 **3.1 SOA formation in PD**

294 We examine the globally and annually averaged RO₂ fate (fRO₂) and the contribution of
295 each reaction pathway to total SOA (fSOA) in PD in Figure 2. To calculate fRO₂, we scale the
296 fRO₂ for individual RO₂ species with the corresponding branching ratios and weight the gridded
297 fRO₂ by RO₂ concentrations (see Text S1 for more details). Only results for ISOP-RO₂ and



298 MTERP-RO₂ are shown because the contribution from BCARY-RO₂ to biogenic SOA is small

299 (less than 1% of total biogenic SOA).



300

301 **Figure 2.** Vertically integrated and globally and annually averaged RO₂ fate (fRO₂; left panel)
 302 weighted by gridded RO₂ concentrations and the percentage contribution of each reaction
 303 pathway to total SOA burden (fSOA; right panel) for MTERP (upper panel) and ISOP (lower
 304 panel). Results are shown for the BASE, NEW_fast, and NEW_slow experiments. Different
 305 reactions are categorized by colors. For ISOP-RO₂, the RO₂+RO₂ reactions include ISOP-RO₂ +
 306 MTERP-RO₂ and ISOP-RO₂ + BCARY-RO₂ reactions (Table 2, part 2), while “Others” include
 307 ISOP-RO₂ decomposition and the reactions with CH₃O₂ and CH₃CO₃. For MTERP-RO₂, the
 308 RO₂ + RO₂ reactions include those between MTERP-RO₂ and ISOP-RO₂, IEPOXOO, MTERP-
 309 RO₂ itself, BCARY-RO₂, and later generations of terpene RO₂ (Table 2, part 2), while the
 310 reactions with NO₃, CH₃O₂, and CH₃CO₃ are included in “Others” (Table 2, part 3). To avoid
 311 double counting, we classify the SOA formed through ISOP-RO₂/BCARY-RO₂ + MTERP-RO₂
 312 solely as MTERP SOA.



313 For MTERP-RO₂, isomerization accounts for ~19% of fRO₂ in the two NEW
314 experiments (Figure 2a). Since we assume that only 22% of MTERP-RO₂ can isomerize, this
315 contribution is substantial, indicating that isomerization is nearly saturated in this branch because
316 the reaction rate of isomerization generally exceeds that of bimolecular reactions (Figure 1). This
317 agrees with Xu et al. (2022), who also found isomerization to be the dominant fate for the
318 MTERP-RO₂ branch that can undergo unimolecular reaction. Isomerization forms a large
319 amount of low volatility products, making it a major contributor to total MTERP SOA formation
320 (46% in NEW_fast and 44% in NEW_slow) (Figure 2b). This highlights the important role of
321 including MTERP-RO₂ isomerization in SOA formation parameterizations.

322 The contribution of MTERP RO₂ + RO₂ reactions to fRO₂ depends on the reactions rates
323 (36% with faster reaction rates in NEW_fast and 17% with slower reaction rates in NEW_slow).
324 However, their contribution to total MTERP SOA is minor (8% in NEW_fast and 3% in
325 NEW_slow) because only 4% of SOAG0 is formed through these reactions. As described in
326 Section 2.2 this is likely a lower limit. Overall, the newly included reactions account for 40 -
327 57% of fRO₂ and 47 - 54% of fSOA in the NEW experiments, significantly modifying the
328 MTERP-RO₂ chemistry from the BASE experiment. MTERP-RO₂ reactions with HO₂ and NO
329 account for 20% and 24% of fRO₂ in NEW_fast, and 31% and 29% in NEW_slow, respectively
330 (Figure 2a). Compared with BASE (fRO₂ for the HO₂ pathway is 62%), the contributions of RO₂
331 + HO₂ to fRO₂ in the NEW experiments are largely supplemented by the isomerization and
332 accretion reactions, which also favor clean conditions. We note that Xu et al. (2022) show a
333 higher RO₂ fate from MTERP-RO₂ + HO₂ reaction, which may indicate different global
334 distributions of NO and VOCs. For fSOA, the contribution from MTERP-RO₂ + HO₂ (31 - 37%)
335 is higher than that from MTERP-RO₂ + NO (15 - 16%), as expected, because products formed



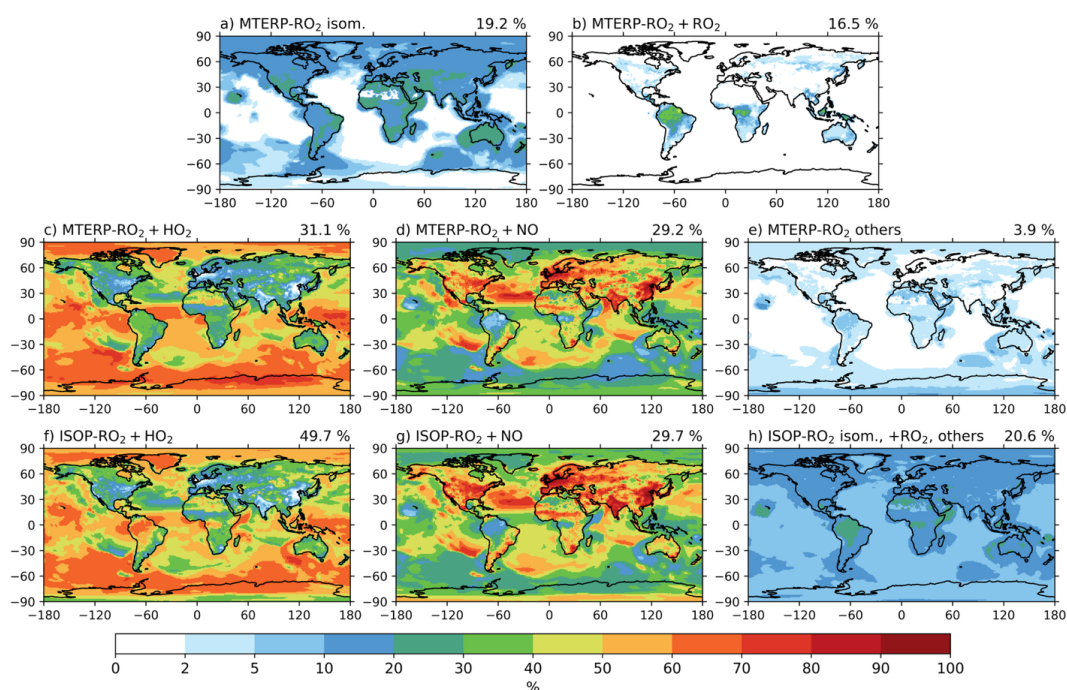
336 through reactions with NO are generally more volatile than those formed through reactions with
337 HO₂.

338 The two NEW experiments have identical isoprene RO₂ chemistry and thus show similar
339 fRO₂ distributions for ISOP-RO₂, with the exception that the NEW_slow has a slightly larger
340 RO₂ + RO₂ fate than NEW_fast due to higher terpene RO₂ concentrations resulting from slower
341 MTERP-RO₂ + RO₂ reaction rates (Figure 2c). In NEW_slow, contributions from RO₂ + HO₂,
342 RO₂ + NO, isomerization, RO₂ + RO₂, and other reactions are 50%, 30%, 11%, 1%, and 9%,
343 respectively. Compared to BASE, the NEW experiments show 20-21% additional RO₂ loss due
344 to the newly introduced reactions. However, these reactions do not produce SOA precursors and
345 thus the relative contributions to ISOP SOA are similar in all three experiments. The
346 contributions to fSOA in NEW_slow from RO₂ + HO₂ and RO₂ + NO are 72% and 28%,
347 respectively.

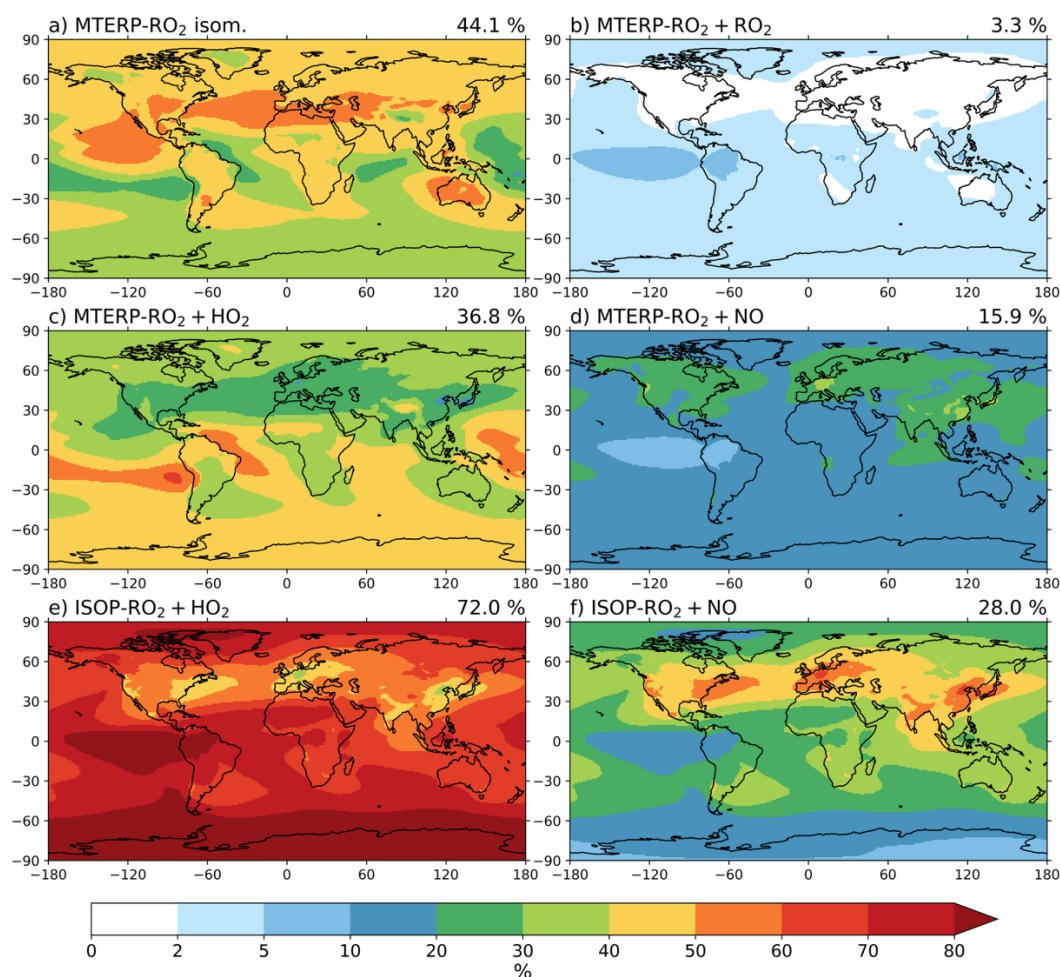
348 The global distributions of fRO₂ from NEW_slow are shown in Figure 3. The
349 contribution from MTERP-RO₂ isomerization is generally spatially uniform over the land, with
350 exceptions over highly polluted environments (e.g., Eastern China), where the isomerization
351 pathway is of little importance (Figure 3a). Its contribution maximizes in North Africa, tropical
352 South America, and Australia, driven by high temperatures over these regions. The MTERP-RO₂
353 + RO₂ reactions contribute significantly (up to 40%) over tropical forests, including the Amazon,
354 Congo Basin, and Southeast Asia (Figure 3b). These regions have strong MTERP emissions and
355 thus high RO₂ concentrations, favoring RO₂ cross and self-reactions. In addition, for both ISOP-
356 RO₂ and MTERP-RO₂, reactions with NO dominate the RO₂ fate over terrestrial polluted regions
357 with high NO emissions, accounting for more than 50% of fRO₂ in the US, most of Eurasia, the
358 Sahel and surrounding areas, and Southern Africa (Figure 3d and 3g). In contrast, RO₂ + HO₂



359 reactions become more important in relatively clean regions, such as the tropical and boreal
 360 forests as well as the ocean (Figure 3c and 3f). Spatial distributions of the annual mean surface
 361 MTERP-RO₂ and ISOP-RO₂ reaction rates are shown in Figures S1 and S2, respectively.



362
 363 **Figure 3.** Vertically integrated and annually averaged fRO_2 in % for MTERP-RO₂ reactions
 364 (panel a-e) and ISOP-RO₂ reactions (panel f-h) from NEW_slow. The sum of reactions for the
 365 same RO₂ (i.e., the sum of a) to e) and f) to h), respectively) is equal to 100%. Global mean fRO_2
 366 weighted by gridded RO₂ concentrations are shown at the top right of each panel.



367
 368 **Figure 4.** Vertically integrated and annually averaged fSOA in % for MTERP-RO₂ reactions
 369 (panel a-d) and ISOP-RO₂ reactions (panel e-f) from NEW_slow. The sum of reactions for the
 370 same RO₂ (i.e., the sum of a) to d) and e) to f), respectively) is equal to 100 %. Global mean
 371 fSOA are shown at the top right of each panel.

372 Figure 4 shows the global distributions of fSOA in NEW_slow. Isomerization accounts
 373 for more than 40% of MTERP SOA in the North Hemisphere and across land in the Southern
 374 Hemisphere (Figure 4a). RO₂ + HO₂ reactions is another major pathway, contributing 20 - 40%
 375 of MTERP SOA formation in the Northern Hemisphere and 30 - 60% in the Southern
 376 Hemisphere (Figure 4c). MTERP-RO₂ + NO contributes 20-40% over the polluted regions in the

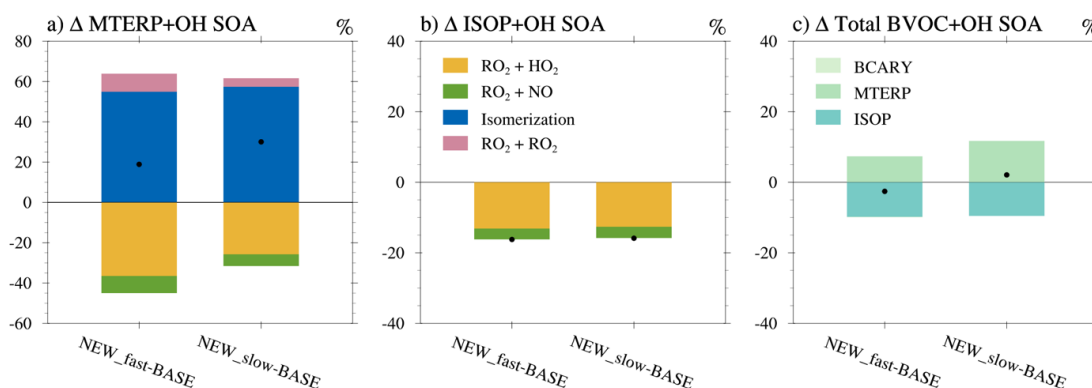


377 Northern Hemisphere but less than 20% elsewhere (Figure 4d). The contribution from MTERP-
378 $\text{RO}_2 + \text{RO}_2$ reactions is minor globally (Figure 4b), due to the small SOA yields and the
379 relatively slow reactions rates. We note that our findings differ from Mayhew et al. (2025) – who
380 identify a critical contribution from the $\text{RO}_2 + \text{RO}_2$ reactions to the SOA in tropical forest
381 regions. The conservative SOA yields for this pathway applied in our simulations may contribute
382 to this discrepancy. Moreover, Mayhew et al. (2025) did not account for isomerization of terpene
383 RO_2 , which may compete with the $\text{RO}_2 + \text{RO}_2$ reactions, and they include the accretion reactions
384 of a broader range of RO_2 species, including those of anthropogenic origin. The different
385 treatments and results from various studies highlight the substantial uncertainties that remain in
386 our understanding of $\text{RO}_2 + \text{RO}_2$ reactions. For ISOP SOA, $\text{RO}_2 + \text{HO}_2$ is responsible for more
387 than 60% of SOA formation most of the globe, except in North America, Europe, and South and
388 East Asia (Figure 4e), where $\text{RO}_2 + \text{NO}$ contributes 40-60% because of the high local NO
389 emissions (Figure 4f).

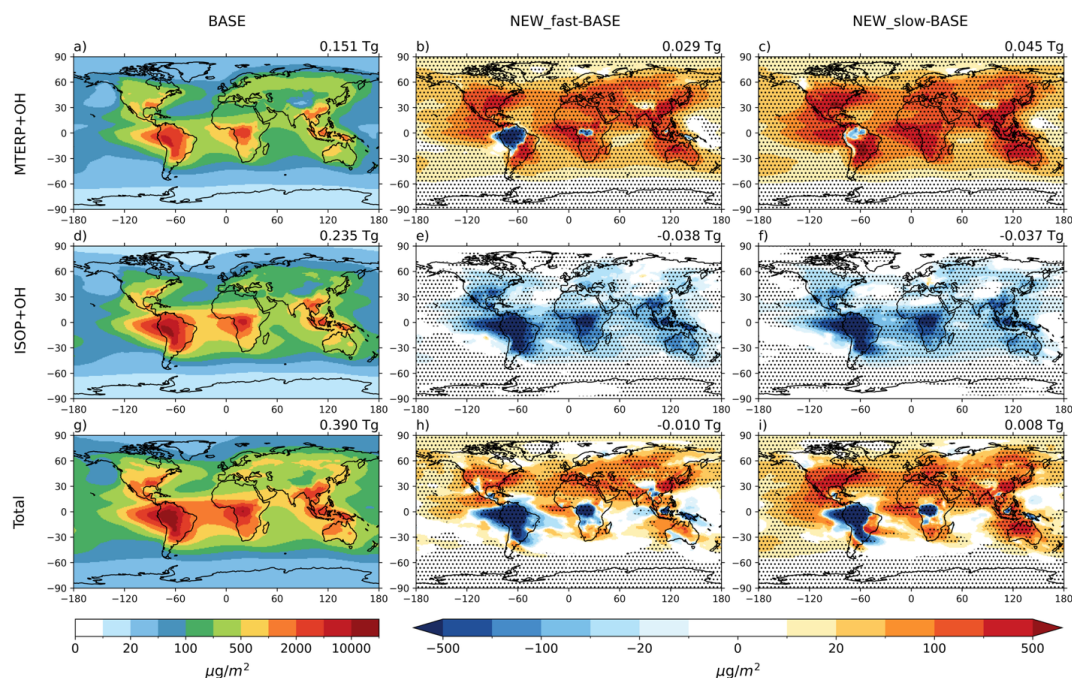
390 The newly added isomerization and $\text{RO}_2 + \text{RO}_2$ reactions compete with the $\text{RO}_2 + \text{HO}_2$
391 and $\text{RO}_2 + \text{NO}$ reactions, leading to decreased MTERP SOA formation through the latter two
392 pathways in the NEW experiments compared with BASE (Figure 5a). At the same time,
393 including isomerization increases MTERP SOA by more than 50%, while the $\text{RO}_2 + \text{RO}_2$
394 reactions account for additional 4-9% increase. The isomerization pathway produces a large
395 amount of low-volatility products and is thus more efficient in SOA formation than the $\text{RO}_2 +$
396 HO_2 and $\text{RO}_2 + \text{NO}$ pathways. Therefore, compared to BASE, total MTERP SOA increases by
397 19 % (0.029 Tg) in NEW_fast and 30 % (0.045 Tg) in NEW_slow. The increase in NEW_slow
398 is higher than that in NEW_fast, because $\text{RO}_2 + \text{HO}_2$ and $\text{RO}_2 + \text{NO}$ contribute more in
399 NEW_slow due to slower $\text{RO}_2 + \text{RO}_2$ reaction rates (Figure 2a), and these two pathways form



400 more SOA than the accretion reaction. The total MTERP SOA increases globally in the two
 401 NEW experiments compared to BASE, except over the Amazon and in Congo Forest in
 402 NEW_fast (Figure 6a-c), where the $\text{RO}_2 + \text{RO}_2$ reactions contribute substantially to the RO_2 fate.
 403 For ISOP SOA, the newly implemented reactions introduce extra losses of ISOP- RO_2 that
 404 compete with the $\text{RO}_2 + \text{HO}_2$ and $\text{RO}_2 + \text{NO}$ reactions but do not form SOA. As a result, the
 405 ISOP SOA decreases by 16 % in the two NEW experiments (0.038 Tg in NEW_fast and 0.037
 406 Tg in NEW_slow) (Figure 5b), and the decrease is globally consistent (Figure 6d-f).



407
 408 **Figure 5.** Percentage changes from BASE to NEW_fast and NEW_slow in the global burden of
 409 a) MTERP + OH SOA and b) ISOP + OH SOA. Different reactions are categorized by colors.
 410 Panel c) shows the percentage change in the total BVOC + OH SOA burden, with VOC
 411 precursors shown in shades of green. The percentages are calculated with respect to BASE.
 412 Black dots in all three panels are global total changes.



413
414 **Figure 6.** Global distributions of SOA column concentrations from BASE (left panel), and the
415 differences between NEW_fast and BASE (middle panel), as well as between NEW_slow and
416 BASE (right panel). Top, middle, and bottom panels show results for SOA burden from MTERP
417 + OH, ISOP + OH, and Total SOA burden from OH oxidation (including BCARY SOA). Dotted
418 regions on the middle and right panels are where the changes are significant to the 0.05 levels.
419 Global average changes in burden are shown above each panel.

420 The increase in MTERP SOA compensates for the ISOP SOA decrease, while the
421 changes in BCARY SOA are small (Figure 5c). As a result, even though the RO₂ chemistry and
422 SOA contribution are significantly altered (Figure 2), total biogenic SOA in the two NEW
423 experiments is similar to that in BASE (< 3% difference). Globally, the NEW experiment
424 predicts a decrease from BASE over the tropical forest regions and an increase over the rest of
425 the world (Figure 6g-i). We note that these results are based on our choices of SOA yields,
426 reaction rates, and branching ratios from various laboratory studies. The measurements from
427 different laboratory studies can vary widely, indicating large uncertainties associated with these
428 results. Moreover, a recent study suggests that previous chamber experiments used to inform



429 SOA yields do not fully represent atmospheric RO₂ fates (Kenagy et al., 2024). Furthermore,
430 Goss et al. (2025) suggest that the reaction conditions and RO₂ fate in many experiments are
431 dynamic and may differ from previous interpretations. In particular, they infer that isomerization
432 was an important RO₂ pathway for previous experiments under low-NO_x conditions used to
433 estimate VBS yields for the RO₂ + HO₂ pathway. This suggests that some isomerization may
434 have already been included in the RO₂ + HO₂ pathway yields, and our newly implemented
435 isomerization pathway may double count these contributions. Overall, these large uncertainties
436 highlight the urgent need to better constrain parameters related to SOA formation in the
437 laboratory.

438 **3.2 Changes in SOA formation from PI to F**

439 Biogenic SOA formation is impacted by biogenic VOC emissions, anthropogenic
440 emissions, and temperature. These factors vary globally over time and thus the biogenic SOA
441 formation can be different from the past to the future. In this section, we examine the RO₂ fate
442 and biogenic SOA formation in PI (1850), PD (2010), and F (2100 following SSP5).

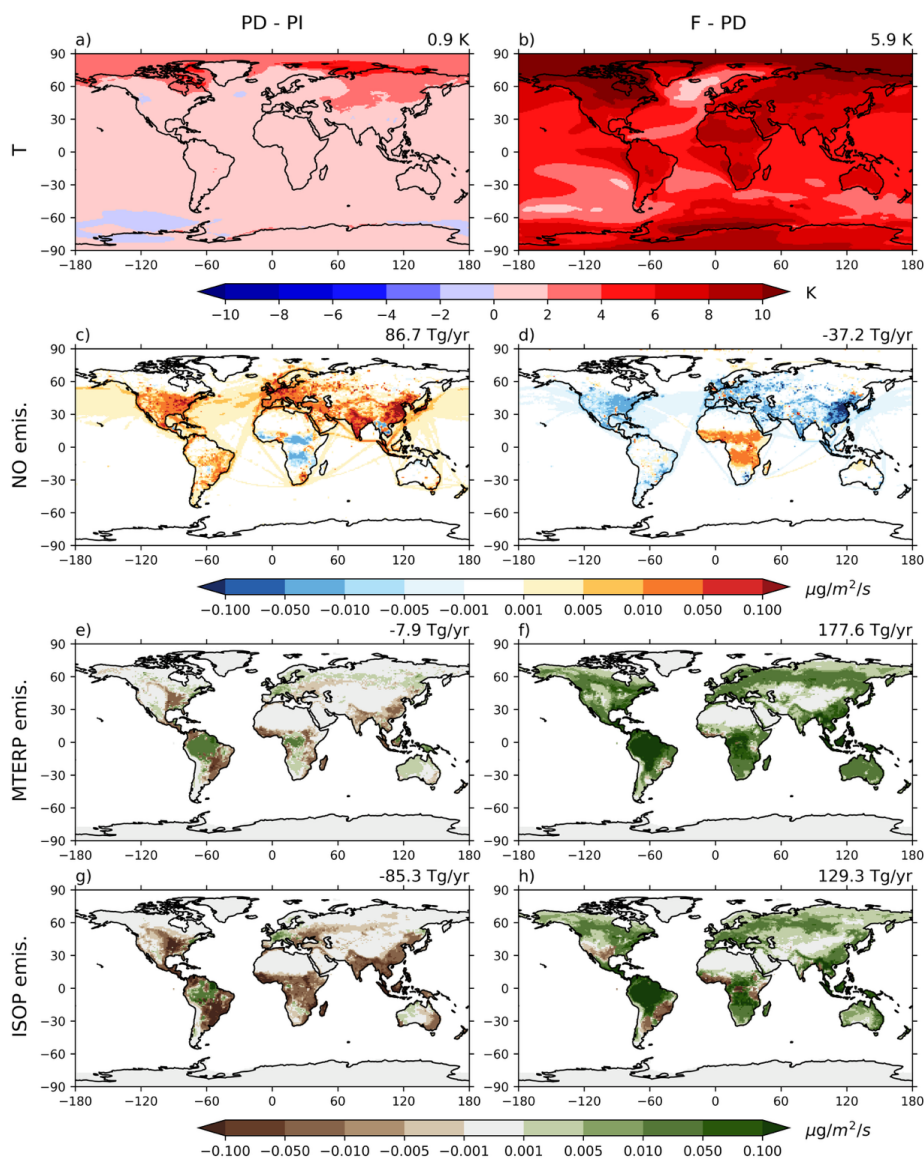
443 Global mean CO₂ mixing ratios in our simulations are 284 ppm, 389 ppm, and 1135 ppm
444 in PI, PD, and F, respectively. In response to the elevated global CO₂ levels, global mean surface
445 temperature increases by 0.9 K from PI to PD and 5.9 K from PD to F (Figure 7a and 7b). The
446 temperature increase is more severe over the Arctic than the rest of the world, which is known as
447 Arctic amplification. The NO emissions increase by 86.7 Tg/yr from PI to PD (78% as compared
448 to PD; all the percentage changes in this section are reported as compared to PD hereafter) and
449 decrease by 37.2 Tg/yr (34%) from PD to F (Figure 7c and 7d). The changes in NO emissions
450 are dominated by changes in anthropogenic emissions. However, North Africa exhibits decreases
451 in NO emissions from PI to PD and increases from PD to F, driven by changes in biomass



452 burning emissions. From PI to PD, global MTERP emissions decrease slightly by 7.9 Tg/yr (6%)
453 (Figure 7e), due to the compensating effects of deforestation and global warming. In contrast,
454 global ISOP emission decrease more substantially (85.3 Tg/yr; 22%) (Figure 7g), because the
455 ISOP emissions are further inhibited by increases in CO₂. BVOC emissions decrease over
456 regions with strong deforestation, including Eastern US, South and East Asia, South America,
457 and Central Africa except the Congo Forest, while the temperature-driven emission increase
458 occurs over the areas with none or little deforestation (e.g., the center of the Amazon forest). The
459 increase over France and Central Europe is related to a local reforestation from PI to PD. In the
460 Congo forest and Southern Africa, MTERP emissions increase over this region in response to
461 temperature increases, while ISOP emissions decrease due to the dominating effect of CO₂
462 inhibition and deforestation. From PD to F, the steep temperature increase in the SSP5 projection
463 results in strong BVOC emission increases – 177.6 Tg/yr (139%) for MTERP emission and
464 129.3 Tg/yr (33%) for ISOP emission (Figure 7f and 7h). The MTERP emissions increase
465 globally despite the impact of the moderate deforestation from PD to F, while localized ISOP
466 emission decreases occur over the US, Central Africa, Brazil, and Argentina due to the
467 deforestation and CO₂ inhibition. We note large uncertainties remain in modeling BVOC
468 emissions (Cao et al., 2021; Guenther et al., 2012), and the predicted changes between different
469 climate conditions may vary depending on whether/how changing vegetation is represented (e.g.
470 Jo et al., 2023). The oxidant levels also vary in response to the changes in NO and VOC
471 emissions (Figure 8). From PI to PD, the surface concentrations of HO_x (i.e., OH and HO₂)
472 generally increase, primarily due to NO emission increase (Figure 8a and 8c). However, in
473 regions characterized by increased NO and decreased VOC emissions (e.g., East US, Europe,
474 and East Asia), the OH-to-HO₂ ratio increases from PI to PD, leading to a reduction in HO₂



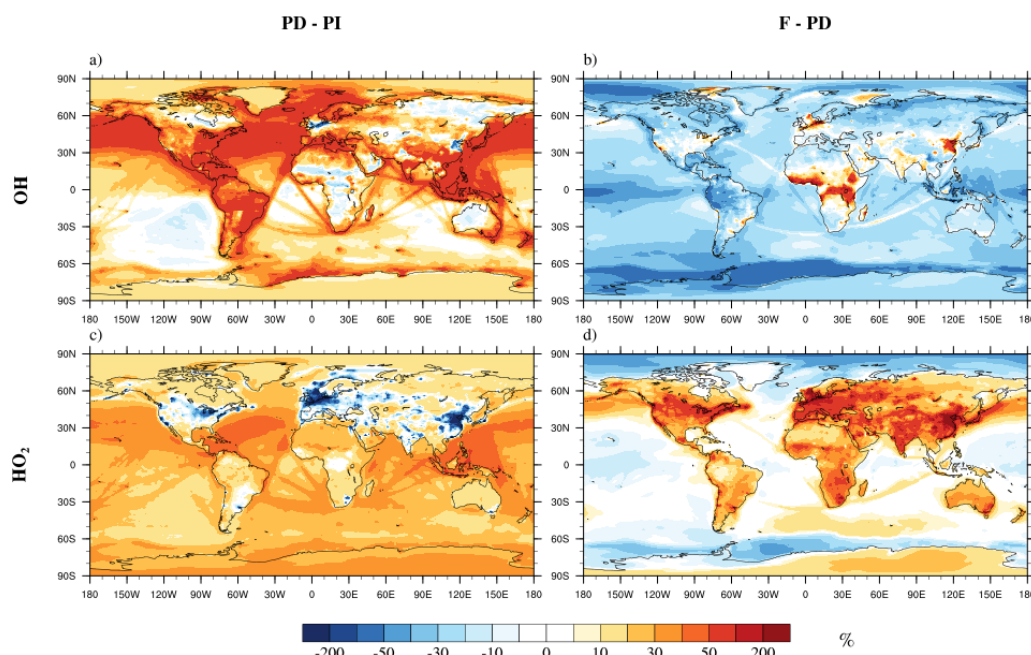
475 concentrations and thus decreasing the $\text{RO}_2 + \text{HO}_2$ fate over these regions. From PD to F, the NO
476 emission decrease and the substantial increase in VOC emissions reduces the OH-to- HO_2 ratio.
477 As a result, OH (HO_2) surface concentrations generally decrease (increase) over land (Figure 8b
478 and 8d). The decrease in OH decreases total OH-initiated SOA formation, while the HO_2
479 increase contributes to a higher $\text{RO}_2 + \text{HO}_2$ fate. The oxidant changes aloft are in general
480 consistent with the surface changes (not shown), except that HO_2 increases slightly over the
481 polluted regions from PI to PD. Other than the abovementioned factors, the emissions of primary
482 organic aerosols increase from PI to PD and decrease from PD to F (not shown), which can
483 impact gas-particle partitioning accordingly.



484

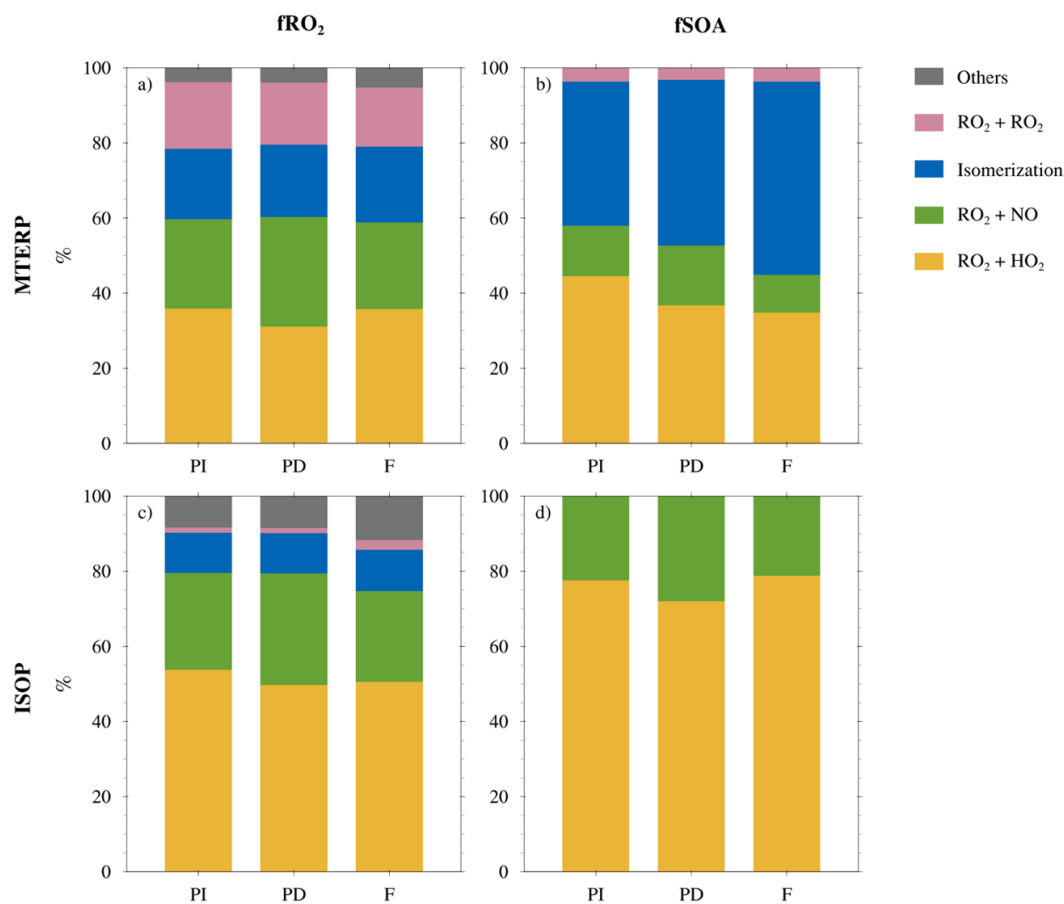
485 **Figure 7.** Global distributions of changes in surface temperatures (first row), NO emissions
 486 (second row), MTERP emissions (third row), and ISOP emissions (fourth row) from PI to PD
 487 (left column) and PD to F (right column). Global average changes in temperatures and global
 488 total changes in emissions are shown above each panel.

489



490
 491 **Figure 8.** Global distributions of percentage changes in surface concentrations of OH (top row)
 492 and HO₂ (bottom row) from PI to PD (left column) and from PD to F (right column). All
 493 percentage changes are calculated with respect to PD levels.

494 The fRO_2 and $fSOA$ for ISOP- RO_2 and MTERP- RO_2 in PI, PD, and F are shown in
 495 Figure 9. Since NO emissions peak in PD, ISOP- RO_2 / MTERP- RO_2 + NO contributes the most
 496 to fRO_2 and $fSOA$ in this period compared to PI and F. Isomerization consistently dominates the
 497 MTERP- RO_2 fate in its branch under all climate conditions – accounting for 19% in PI and PD,
 498 and slightly higher in F with 20% due to the extreme warming that further accelerates this
 499 pathway in F (Figure 9a). Its contribution to total MTERP SOA is substantial and increases from
 500 38% in PI to 44% in PD and further to 51% in F (Figure 9b), highlighting the critical role of
 501 MTERP isomerization to SOA formation across all climate conditions. The isomerization $fSOA$
 502 increases from PI to PD and to F reflect not only the fRO_2 , but also how SOA volatility responds
 503 to temperature changes (i.e. the gas-phase is favored under higher temperatures for more semi-
 504 volatile SOA), which favors the contribution from isomerization.

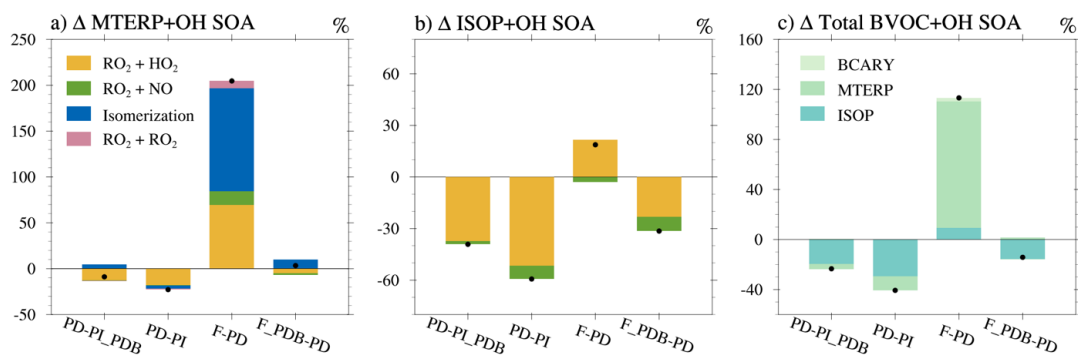


505
 506 **Figure 9.** Same as Figure 2, except that results are shown for PI, PD, and F climate conditions.
 507 All the experiments follow the same RO₂ chemistry as in NEW_slow.

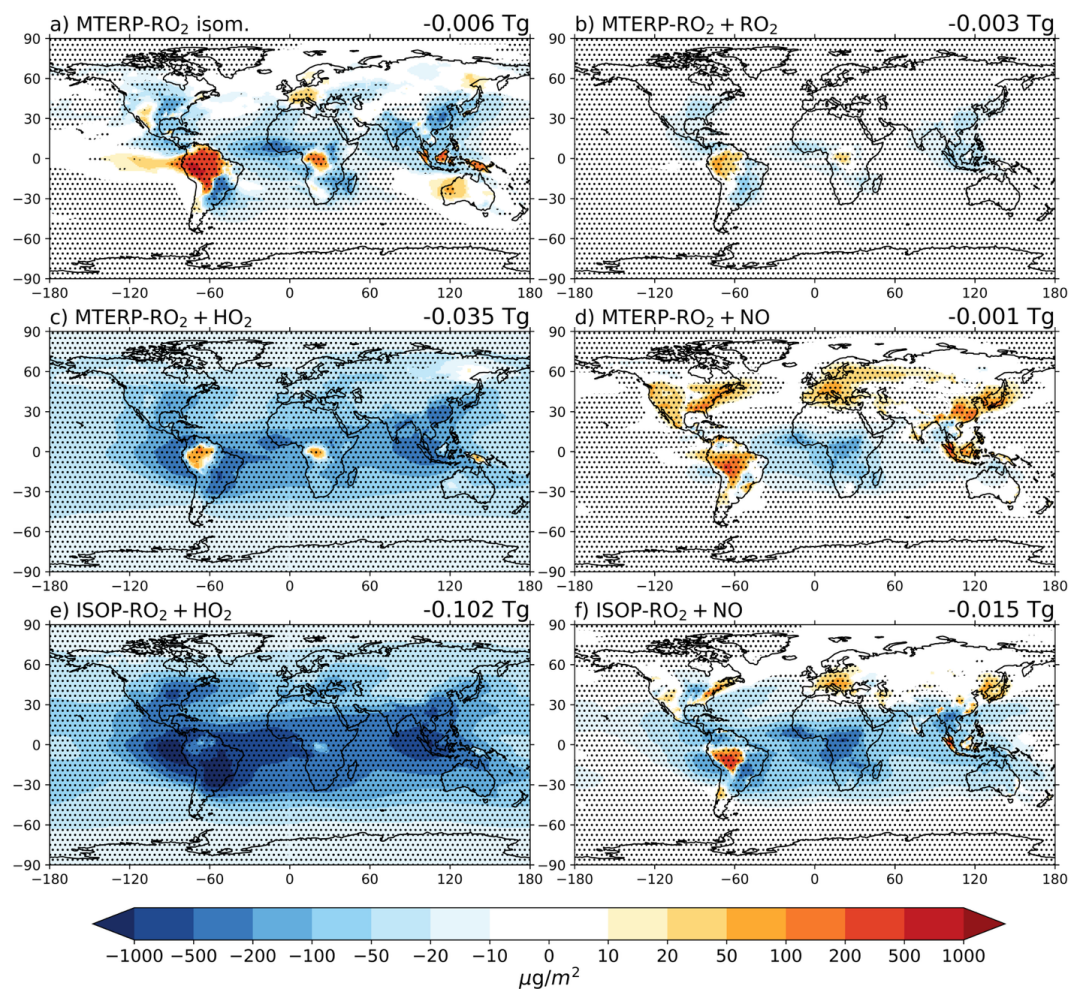
508 From PI to PD, the MTERP and ISOP SOA burden decreases by 23% (0.045 Tg) and
 509 59% (0.117 Tg), respectively (Figure 10a and 10b). The global distributions of SOA burden
 510 changes generally follow the changes in BVOC emissions (Figures 11, 7e, and 7g), except for
 511 the RO₂ + NO pathway. The changes in SOA formed through the MTERP-RO₂ + NO pathway
 512 are associated with changes in NO emissions (Figures 11d and 7c), driven by the influence of
 513 NO on both RO₂ chemistry (Figure 9a) and OH concentrations (Figure 8a). The impacts of NO
 514 emission changes on SOA formed through ISOP-RO₂ + NO is also evident over the west coast of



515 the US, East Asia, and Southeast Asia, despite the strong ISOP emission decrease (Figure 11f).
 516 The decrease in MTERP and ISOP SOA burden are both dominated by the reduction in the RO₂
 517 + HO₂ pathway (Figure 10a and 10b), which is caused by VOC emission decreases (Figure 7e
 518 and 7g) and higher NO fate in PD (Figure 9a and 9c). The shift in RO₂ fate from RO₂ + HO₂ to
 519 RO₂ + NO reduces SOA formed through bimolecular reactions, since the products from the latter
 520 pathway are more volatile. In addition, the overall SOA decrease results in less condensation,
 521 which further decreases SOA burden. As a result, the decrease in SOA burden is stronger than
 522 that in the corresponding VOC emissions.



523 **Figure 10.** Same as Figure 5, except showing historical and future changes in SOA burden. All
 524 the percentages are calculated with respect to PD.
 525

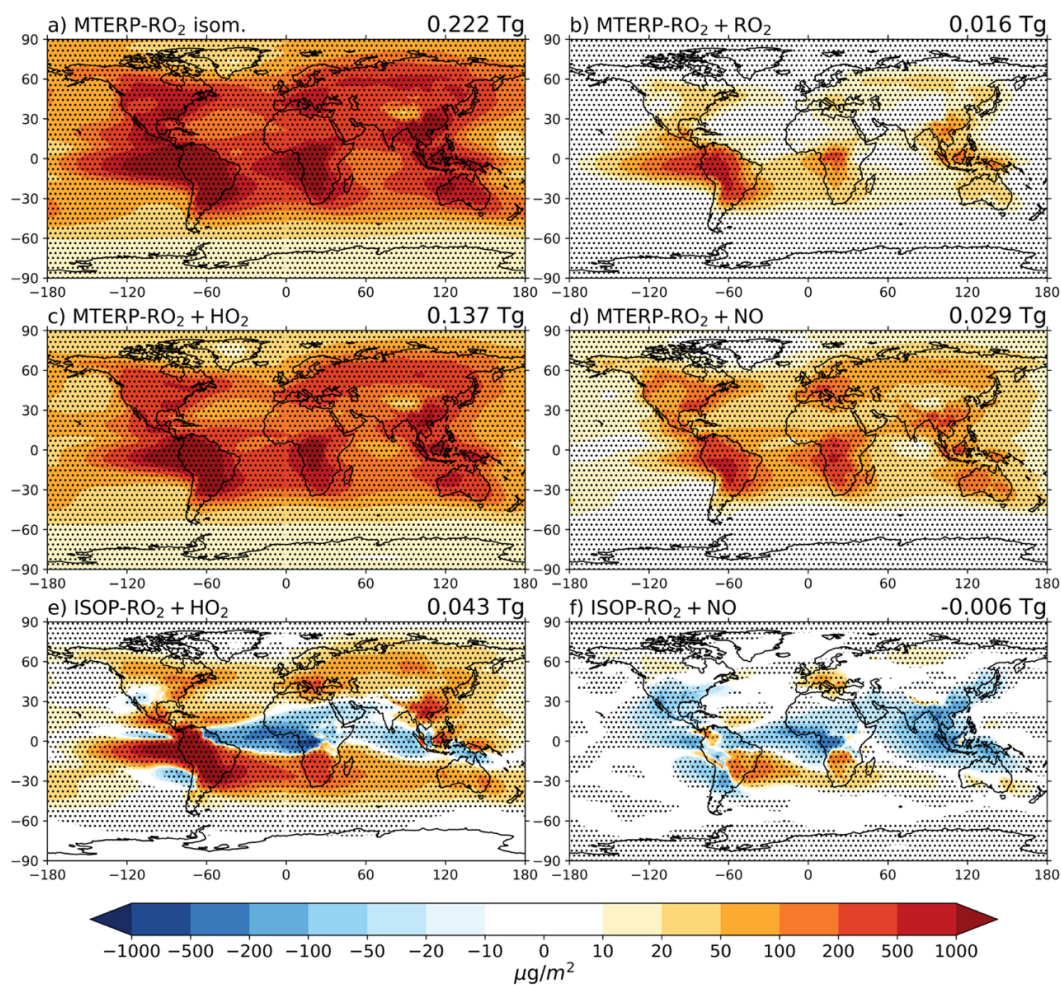


526
 527 **Figure 11.** Changes in annual mean SOA column concentrations from PI to PD through a)
 528 MTERP-RO₂ isomerization, b) MTERP-RO₂ + RO₂, c) MTERP-RO₂ + HO₂, d) MTERP-RO₂ +
 529 NO, e) ISOP-RO₂ + HO₂, f) ISOP-RO₂ + NO reaction pathways. Dotted regions are where the
 530 changes are significant to the 0.05 levels. Global changes in total burden are shown above each
 531 panel.

532 From PD to F, the substantial increase in MTERP emissions enhances SOA formation via
 533 all RO₂ pathways globally (Figure 7f, 10a, and 12a-d). This increase in SOA promotes additional
 534 condensation, which in turn further amplifies SOA production. However, the warming in F tends
 535 to push the gas-particle partitioning towards gas phase and reduces the condensation of precursor
 536 gases, partly offsetting the SOA increase. Overall, the MTERP SOA burden increases by 205%



537 (0.403 Tg) (Figure 10a). Isomerization is the dominant contributor to this increase, because the
 538 low volatility products it forms are less prone to evaporation under increasing temperature. The
 539 total ISOP SOA increases by 19% (0.037 Tg) from PD to F (Figure 10b). This is dominated by
 540 the increase in SOA formed through the $\text{RO}_2 + \text{HO}_2$ pathway (Figure 12e), which is driven by
 541 ISOP emission increases (Figure 7h) and a shift in RO_2 fate from the $\text{RO}_2 + \text{NO}$ pathway toward
 542 the $\text{RO}_2 + \text{HO}_2$ pathway (Figure 9c) due to reductions in NO emissions and increases in HO_2
 543 concentrations from PD to F (Figures 7d and 8d).



544
 545 **Figure 12.** Same as Figure 11, except for changes from PD to F.



546 Overall, the total BVOC SOA decreases by 41% (0.162 Tg) from PI to PD, mainly due to
547 reductions in ISOP SOA (Figure 10c). In contrast, from PD to F, it increases by 113% (0.451
548 Tg), primarily due to enhanced MTERP SOA. These changes are largely driven by changes in
549 BVOC emissions, with contributions from changes in RO₂ chemical fate and gas-particle
550 partitioning.

551 To further isolate how the chemistry is perturbed in different climate conditions, we
552 compare PD with PI_PDB and F_PDB (Figure 10) – these two experiments are the same as PI
553 and F, respectively, but have VOC emissions fixed at the PD level (see details in Section 2.4).
554 When removing the impacts of BVOC emission changes, MTERP SOA from isomerization
555 increases from both PI_PDB to PD and PD to F_PDB, reflecting the acceleration of MTERP-
556 RO₂ isomerization with increasing temperatures. In contrast, the SOA formed through
557 bimolecular reactions declines continuously from the past to the present and the future. The
558 decrease from PI_PDB to PD is mainly due to the decreased SOA formation through the RO₂ +
559 HO₂ pathway as a result of the shift of RO₂ fate under higher NO emissions in PD, while the
560 reduction from PD to F_PDB results from stronger warming that shifts gas-particle partitioning
561 toward the gas phase. Overall, about half of the simulated decrease in total biogenic SOA from
562 PI to PD is due to chemistry and thermodynamics (23% from PI_PDB to PD compared to 41%
563 from PI to PD; Figure 10c). Chemical and thermodynamics factors lead to a moderate decrease
564 (14%) from PD to F_PDB (Figure 10c); this effect is overwhelmed by the increase in BVOC
565 emissions from PD to F.



566 4. Conclusions

567 In this study, we expand the biogenic SOA formation mechanism in CESM2.2 based on
568 the latest understanding of RO₂ chemistry. Specifically, we implement the isomerization and
569 RO₂ + RO₂ reaction pathways for terpene SOA formation and add isoprene product reactions
570 included in MOZART but absent from the standard VBS. Both fast and slow RO₂ + RO₂ reaction
571 rates combinations are tested.

572 We find that MTERP isomerization plays a critical role in SOA formation. The RO₂
573 branch capable of isomerization is nearly saturated due to its fast reaction rate and this pathway
574 contributes almost half of MTERP SOA formation by producing large amounts of low-volatility
575 products. The RO₂ + RO₂ reactions contribute moderately to the MTERP RO₂ fate but make a
576 minor contribution to the MTERP SOA formation. The updated RO₂ chemistry increases
577 MTERP SOA by 19 - 30% compared with the baseline configuration, mainly due to the
578 isomerization pathway. In addition, because of extra RO₂ loss introduced by the newly
579 implemented reactions, the ISOP SOA decreases by 16%. The increase in MTERP SOA and the
580 decrease in ISOP SOA compensate for each other. As a result, the total biogenic SOA burden is
581 similar in the baseline and new configurations, despite the substantial changes in RO₂ chemistry
582 and SOA formation pathways.

583 With the new chemistry, we investigate how the RO₂ fate and the SOA formation varies
584 from the past to the present and the future. We find that for MTERP, the isomerization pathway
585 is nearly saturated under all climate conditions, with a higher contribution in F because of the
586 extreme global warming that further accelerates this pathway. The contribution from the RO₂ +
587 NO pathway to both the RO₂ fate and SOA formation peaks in PD, due to higher NO emissions
588 in PD than PI and F. The total biogenic SOA decreases by nearly half from PI to PD and is



589 doubled from PD to F. The changes in SOA are dominated by changes in BVOC emissions, with
590 contributions from shifts in RO₂ chemical fate and gas-particle partitioning playing a more
591 important role in the changes from PI to PD.

592 We simulate large changes in the fate of biogenic RO₂ and SOA burden from the past to
593 the future. RO₂ chemistry plays an important role in determining SOA formation but is still
594 subject to substantial uncertainties. To improve the representation of SOA in 3D models and
595 better quantify their climate impacts, more laboratory studies are needed to constrain the
596 uncertainties on the reaction rates and SOA yields for isomerization and RO₂ + RO₂ reactions as
597 well as the isomerization branching ratio. Additional work is needed to translate laboratory SOA
598 yields into model parameterizations that balance chemical complexity with computational
599 efficiency.

600 **Code and data availability**

601 This work is based on CESM2.2 (NCAR, 2023). The modified chemical mechanisms and
602 the data shown in the figures are available on Zenodo (Shi et al., 2026). This Zenodo link will be
603 available once the paper accepted.

604 **Author contributions**

605 YS, CLH, and JHK formulated the overarching research goals and aims. YS and CLH
606 designed the methodology. YS developed the model code, performed the simulations, analyzed
607 the results, and created the figures. YS and CLH wrote the initial draft of this paper. All authors
608 reviewed this paper.



609 **Competing interests**

610 The contact authors declare no competing interest.

611 **Acknowledgements**

612 We acknowledge high-performance computing support from the Derecho system
613 (doi:10.5065/qx9a-pg09) provided by the NSF National Center for Atmospheric Research
614 (NCAR), sponsored by the National Science Foundation.

615 **Financial support**

616 This work was supported by the U.S. Department of Energy (DE-SC0022017) grant to
617 CLH and JHK at MIT. YS also acknowledge the support of the Pacific Northwest National
618 Laboratory Linus Pauling Distinguished Postdoctoral Fellowship program (Proposal Scope
619 86140). The Pacific Northwest National Laboratory (PNNL) is operated for DOE by the Battelle
620 Memorial Institute under contract no. DE-AC06-76RLO1830.

621 **References**

622 Arneth, A., Miller, P. A., Scholze, M., Hickler, T., Schurgers, G., Smith, B., and Prentice, I. C.:
623 CO₂ inhibition of global terrestrial isoprene emissions: Potential implications for
624 atmospheric chemistry, *Geophys. Res. Lett.*, 34, <https://doi.org/10.1029/2007GL030615>,
625 2007.

626 Baboomian, V. J., Gu, Y., and Nizkorodov, S. A.: Photodegradation of Secondary Organic
627 Aerosols by Long-Term Exposure to Solar Actinic Radiation, *ACS Earth Space Chem.*, 4,
628 1078–1089, <https://doi.org/10.1021/acsearthspacechem.0c00088>, 2020.



- 629 Bates, K. H. and Jacob, D. J.: A new model mechanism for atmospheric oxidation of isoprene:
630 global effects on oxidants, nitrogen oxides, organic products, and secondary organic
631 aerosol, *Atmospheric Chemistry and Physics*, 19, 9613–9640, [https://doi.org/10.5194/acp-](https://doi.org/10.5194/acp-19-9613-2019)
632 19-9613-2019, 2019.
- 633 Bergman, T., Makkonen, R., Schrödner, R., Swietlicki, E., Phillips, V. T. J., Le Sager, P., and van
634 Noije, T.: Description and evaluation of a secondary organic aerosol and new particle
635 formation scheme within TM5-MP v1.2, *Geoscientific Model Development*, 15, 683–713,
636 <https://doi.org/10.5194/gmd-15-683-2022>, 2022.
- 637 Berndt, T., Mentler, B., Scholz, W., Fischer, L., Herrmann, H., Kulmala, M., and Hansel, A.:
638 Accretion Product Formation from Ozonolysis and OH Radical Reaction of α -Pinene:
639 Mechanistic Insight and the Influence of Isoprene and Ethylene, *Environ. Sci. Technol.*,
640 52, 11069–11077, <https://doi.org/10.1021/acs.est.8b02210>, 2018a.
- 641 Berndt, T., Scholz, W., Mentler, B., Fischer, L., Herrmann, H., Kulmala, M., and Hansel, A.:
642 Accretion Product Formation from Self- and Cross-Reactions of RO₂ Radicals in the
643 Atmosphere, *Angewandte Chemie International Edition*, 57, 3820–3824,
644 <https://doi.org/10.1002/anie.201710989>, 2018b.
- 645 Berndt, T., Hoffmann, E. H., Tilgner, A., and Herrmann, H.: Highly oxidized products from the
646 atmospheric reaction of hydroxyl radicals with isoprene, *Nat Commun*, 16, 2068,
647 <https://doi.org/10.1038/s41467-025-57336-1>, 2025.
- 648 Bianchi, F., Kurtén, T., Riva, M., Mohr, C., Rissanen, M. P., Roldin, P., Berndt, T., Crounse, J.
649 D., Wennberg, P. O., Mentel, T. F., Wildt, J., Junninen, H., Jokinen, T., Kulmala, M.,
650 Worsnop, D. R., Thornton, J. A., Donahue, N., Kjaergaard, H. G., and Ehn, M.: Highly
651 Oxygenated Organic Molecules (HOM) from Gas-Phase Autoxidation Involving Peroxy



- 652 Radicals: A Key Contributor to Atmospheric Aerosol, *Chem. Rev.*, 119, 3472–3509,
653 <https://doi.org/10.1021/acs.chemrev.8b00395>, 2019.
- 654 Borchert, J. E., Salo, V.-T., Golin Almeida, T., and Kjaergaard, H. G.: Hydrogen Shift Reactions
655 in Nonhydrocarbon Peroxy Radicals, *J. Phys. Chem. A*, 130, 1375–1383,
656 <https://doi.org/10.1021/acs.jpca.5c06832>, 2026.
- 657 Burnett, R., Chen, H., Szyszkowicz, M., Fann, N., Hubbell, B., Pope, C. A., Apte, J. S., Brauer,
658 M., Cohen, A., Weichenthal, S., Coggins, J., Di, Q., Brunekreef, B., Frostad, J., Lim, S. S.,
659 Kan, H., Walker, K. D., Thurston, G. D., Hayes, R. B., Lim, C. C., Turner, M. C., Jerrett,
660 M., Krewski, D., Gapstur, S. M., Diver, W. R., Ostro, B., Goldberg, D., Crouse, D. L.,
661 Martin, R. V., Peters, P., Pinault, L., Tjepkema, M., van Donkelaar, A., Villeneuve, P. J.,
662 Miller, A. B., Yin, P., Zhou, M., Wang, L., Janssen, N. A. H., Marra, M., Atkinson, R. W.,
663 Tsang, H., Quoc Thach, T., Cannon, J. B., Allen, R. T., Hart, J. E., Laden, F., Cesaroni, G.,
664 Forastiere, F., Weinmayr, G., Jaensch, A., Nagel, G., Concin, H., and Spadaro, J. V.:
665 Global estimates of mortality associated with long-term exposure to outdoor fine
666 particulate matter, *Proceedings of the National Academy of Sciences*, 115, 9592–9597,
667 <https://doi.org/10.1073/pnas.1803222115>, 2018.
- 668 Cao, Y., Yue, X., Liao, H., Yang, Y., Zhu, J., Chen, L., Tian, C., Lei, Y., Zhou, H., and Ma, Y.:
669 Ensemble projection of global isoprene emissions by the end of 21st century using CMIP6
670 models, *Atmospheric Environment*, 267, 118766,
671 <https://doi.org/10.1016/j.atmosenv.2021.118766>, 2021.
- 672 Chin, M., Ginoux, P., Kinne, S., Torres, O., Holben, B. N., Duncan, B. N., Martin, R. V., Logan,
673 J. A., Higurashi, A., and Nakajima, T.: Tropospheric Aerosol Optical Thickness from the
674 GOCART Model and Comparisons with Satellite and Sun Photometer Measurements,



- 675 Journal of the Atmospheric Sciences, 59, 461–483, <https://doi.org/10.1175/1520->
676 0469(2002)059%253C0461:TAOTFT%253E2.0.CO;2, 2002.
- 677 Chung, S. H. and Seinfeld: Global distribution and climate forcing of carbonaceous aerosols, J.
678 Geophys. Res., 107, 4407, <https://doi.org/10.1029/2001JD001397>, 2002.
- 679 Colarco, P., Da Silva, A., Chin, M., and Diehl, T.: Online simulations of global aerosol
680 distributions in the NASA GEOS-4 model and comparisons to satellite and ground-based
681 aerosol optical depth, J. Geophys. Res., 115, 2009JD012820,
682 <https://doi.org/10.1029/2009JD012820>, 2010.
- 683 Dada, L., Stolzenburg, D., Simon, M., Fischer, L., Heinritzi, M., Wang, M., Xiao, M., Vogel, A.
684 L., Ahonen, L., Amorim, A., Baalbaki, R., Baccarini, A., Baltensperger, U., Bianchi, F.,
685 Daellenbach, K. R., DeVivo, J., Dias, A., Dommen, J., Duplissy, J., Finkenzeller, H.,
686 Hansel, A., He, X.-C., Hofbauer, V., Hoyle, C. R., Kangasluoma, J., Kim, C., Kürten, A.,
687 Kvashnin, A., Mauldin, R., Makhmutov, V., Marten, R., Mentler, B., Nie, W., Petäjä, T.,
688 Quéléver, L. L. J., Saathoff, H., Tauber, C., Tome, A., Molteni, U., Volkamer, R., Wagner,
689 R., Wagner, A. C., Wimmer, D., Winkler, P. M., Yan, C., Zha, Q., Rissanen, M., Gordon,
690 H., Curtius, J., Worsnop, D. R., Lehtipalo, K., Donahue, N. M., Kirkby, J., El Haddad, I.,
691 and Kulmala, M.: Role of sesquiterpenes in biogenic new particle formation, Science
692 Advances, 9, eadi5297, <https://doi.org/10.1126/sciadv.adi5297>, 2023.
- 693 D’Ambro, E. L., Møller, K. H., Lopez-Hilfiker, F. D., Schobesberger, S., Liu, J., Shilling, J. E.,
694 Lee, B. H., Kjaergaard, H. G., and Thornton, J. A.: Isomerization of Second-Generation
695 Isoprene Peroxy Radicals: Epoxide Formation and Implications for Secondary Organic
696 Aerosol Yields, Environ. Sci. Technol., 51, 4978–4987,
697 <https://doi.org/10.1021/acs.est.7b00460>, 2017.



698 Danabasoglu, G., Lamarque, J.-F., Bacmeister, J., Bailey, D. A., DuVivier, A. K., Edwards, J.,
699 Emmons, L. K., Fasullo, J., Garcia, R., Gettelman, A., Hannay, C., Holland, M. M., Large,
700 W. G., Lauritzen, P. H., Lawrence, D. M., Lenaerts, J. T. M., Lindsay, K., Lipscomb, W.
701 H., Mills, M. J., Neale, R., Oleson, K. W., Otto-Bliesner, B., Phillips, A. S., Sacks, W.,
702 Tilmes, S., van Kampenhout, L., Vertenstein, M., Bertini, A., Dennis, J., Deser, C., Fischer,
703 C., Fox-Kemper, B., Kay, J. E., Kinnison, D., Kushner, P. J., Larson, V. E., Long, M. C.,
704 Mickelson, S., Moore, J. K., Nienhouse, E., Polvani, L., Rasch, P. J., and Strand, W. G.:
705 The Community Earth System Model Version 2 (CESM2), *Journal of Advances in*
706 *Modeling Earth Systems*, 12, e2019MS001916, <https://doi.org/10.1029/2019MS001916>,
707 2020.

708 Ehn, M., Thornton, J. A., Kleist, E., Sipilä, M., Junninen, H., Pullinen, I., Springer, M., Rubach,
709 F., Tillmann, R., Lee, B., Lopez-Hilfiker, F., Andres, S., Acir, I.-H., Rissanen, M., Jokinen,
710 T., Schobesberger, S., Kangasluoma, J., Kontkanen, J., Nieminen, T., Kurtén, T., Nielsen,
711 L. B., Jørgensen, S., Kjaergaard, H. G., Canagaratna, M., Maso, M. D., Berndt, T., Petäjä,
712 T., Wahner, A., Kerminen, V.-M., Kulmala, M., Worsnop, D. R., Wildt, J., and Mentel, T.
713 F.: A large source of low-volatility secondary organic aerosol, *Nature*, 506, 476–479,
714 <https://doi.org/10.1038/nature13032>, 2014.

715 Emmons, L. K., Schwantes, R. H., Orlando, J. J., Tyndall, G., Kinnison, D., Lamarque, J., Marsh,
716 D., Mills, M. J., Tilmes, S., Bardeen, C., Buchholz, R. R., Conley, A., Gettelman, A.,
717 Garcia, R., Simpson, I., Blake, D. R., Meinardi, S., and Pétron, G.: The Chemistry
718 Mechanism in the Community Earth System Model Version 2 (CESM2), *J. Adv. Model.*
719 *Earth Syst.*, 12, <https://doi.org/10.1029/2019MS001882>, 2020.



- 720 Forster, P., T. Storelvmo, K. Armour, W. Collins, J.-L. Dufresne, D. Frame, D.J. Lunt, T.
721 Mauritsen, M.D. Palmer, M. Watanabe, M. Wild, and H. Zhang: The Earth's Energy
722 Budget, Climate Feedbacks, and Climate Sensitivity, in *Climate Change 2021: The*
723 *Physical Science Basis. Contribution of Working Group I to the Sixth Assessment Report*
724 *of the Intergovernmental Panel on Climate Change*, edited by Masson-Delmotte, V., P.
725 Zhai, A. Pirani, S.L. Connors, C. Péan, S. Berger, N. Caud, Y. Chen, L. Goldfarb, M.I.
726 Gomis, M. Huang, K. Leitzell, E. Lonnoy, J.B.R. Matthews, T.K. Maycock, T. Waterfield,
727 O. Yelekçi, R. Yu, and B. Zhou, Cambridge University Press, Cambridge, United Kingdom
728 and New York, NY, USA, 923–1054, <https://doi.org/10.1017/9781009157896.009>, 2011
- 729 Goss, M. B., Kenagy, H. S., Heald, C. L., and Kroll, J. H.: Re-examining chemical conditions of
730 past chamber studies of secondary organic aerosol formation,
731 <https://doi.org/10.26434/chemrxiv-2025-1xq6q>, 3 April 2025a.
- 732 Goss, M. B., Kenagy, H. S., Heald, C. L., and Kroll, J. H.: Re-Examining Chemical Conditions of
733 Past Chamber Studies of Secondary Organic Aerosol Formation, *ACS EST Air*, 2, 2117–
734 2130, <https://doi.org/10.1021/acsestair.5c00112>, 2025b.
- 735 Guenther, A. B., Jiang, X., Heald, C. L., Sakulyanontvittaya, T., Duhl, T., Emmons, L. K., and
736 Wang, X.: The Model of Emissions of Gases and Aerosols from Nature version 2.1
737 (MEGAN2.1): an extended and updated framework for modeling biogenic emissions,
738 *Geoscientific Model Development*, 5, 1471–1492, [https://doi.org/10.5194/gmd-5-1471-](https://doi.org/10.5194/gmd-5-1471-2012)
739 2012, 2012.
- 740 Hallquist, M., Wenger, J. C., Baltensperger, U., Rudich, Y., Simpson, D., Claeys, M., Dommen,
741 J., Donahue, N. M., George, C., Goldstein, A. H., Hamilton, J. F., Herrmann, H.,
742 Hoffmann, T., Iinuma, Y., Jang, M., Jenkin, M. E., Jimenez, J. L., Kiendler-Scharr, A.,



- 743 Maenhaut, W., McFiggans, G., Mentel, T. F., Monod, A., Prévôt, A. S. H., Seinfeld, J. H.,
744 Surratt, J. D., Szmigielski, R., and Wildt, J.: The formation, properties and impact of
745 secondary organic aerosol: current and emerging issues, *Atmospheric Chemistry and*
746 *Physics*, 9, 5155–5236, <https://doi.org/10.5194/acp-9-5155-2009>, 2009.
- 747 Heald, C. L. and Geddes, J. A.: The impact of historical land use change from 1850 to 2000 on
748 secondary particulate matter and ozone, *Atmos. Chem. Phys.*, 16, 14997–15010,
749 <https://doi.org/10.5194/acp-16-14997-2016>, 2016.
- 750 Heald, C. L., Wilkinson, M. J., Monson, R. K., Alo, C. A., Wang, G., and Guenther, A.: Response
751 of isoprene emission to ambient CO₂ changes and implications for global budgets, *Global*
752 *Change Biology*, 15, 1127–1140, <https://doi.org/10.1111/j.1365-2486.2008.01802.x>,
753 2009.
- 754 Henry, K. M. and Donahue, N. M.: Photochemical Aging of α -Pinene Secondary Organic Aerosol:
755 Effects of OH Radical Sources and Photolysis, *J. Phys. Chem. A*, 116, 5932–5940,
756 <https://doi.org/10.1021/jp210288s>, 2012.
- 757 Hodzic, A., Madronich, S., Kasibhatla, P. S., Tyndall, G., Aumont, B., Jimenez, J. L., Lee-Taylor,
758 J., and Orlando, J.: Organic photolysis reactions in tropospheric aerosols: effect on
759 secondary organic aerosol formation and lifetime, *Atmospheric Chemistry and Physics*, 15,
760 9253–9269, <https://doi.org/10.5194/acp-15-9253-2015>, 2015.
- 761 Hodzic, A., Kasibhatla, P. S., Jo, D. S., Cappa, C. D., Jimenez, J. L., Madronich, S., and Park, R.
762 J.: Rethinking the global secondary organic aerosol (SOA) budget: stronger production,
763 faster removal, shorter lifetime, *Atmos. Chem. Phys.*, 16, 7917–7941,
764 <https://doi.org/10.5194/acp-16-7917-2016>, 2016.



- 765 Hoyle, C. R., Berntsen, T., Myhre, G., and Isaksen, I. S. A.: Secondary organic aerosol in the
766 global aerosol – chemical transport model Oslo CTM2, *Atmospheric Chemistry and*
767 *Physics*, 7, 5675–5694, <https://doi.org/10.5194/acp-7-5675-2007>, 2007.
- 768 Jimenez, J. L., Canagaratna, M. R., Donahue, N. M., Prevot, A. S. H., Zhang, Q., Kroll, J. H.,
769 DeCarlo, P. F., Allan, J. D., Coe, H., Ng, N. L., Aiken, A. C., Docherty, K. S., Ulbrich, I.
770 M., Grieshop, A. P., Robinson, A. L., Duplissy, J., Smith, J. D., Wilson, K. R., Lanz, V.
771 A., Hueglin, C., Sun, Y. L., Tian, J., Laaksonen, A., Raatikainen, T., Rautiainen, J.,
772 Vaattovaara, P., Ehn, M., Kulmala, M., Tomlinson, J. M., Collins, D. R., Cubison, M. J.,
773 E., Dunlea, J., Huffman, J. A., Onasch, T. B., Alfarra, M. R., Williams, P. I., Bower, K.,
774 Kondo, Y., Schneider, J., Drewnick, F., Borrmann, S., Weimer, S., Demerjian, K., Salcedo,
775 D., Cottrell, L., Griffin, R., Takami, A., Miyoshi, T., Hatakeyama, S., Shimono, A., Sun,
776 J. Y., Zhang, Y. M., Dzepina, K., Kimmel, J. R., Sueper, D., Jayne, J. T., Herndon, S. C.,
777 Trimborn, A. M., Williams, L. R., Wood, E. C., Middlebrook, A. M., Kolb, C. E.,
778 Baltensperger, U., and Worsnop, D. R.: Evolution of Organic Aerosols in the Atmosphere,
779 *Science*, 326, 1525–1529, <https://doi.org/10.1126/science.1180353>, 2009.
- 780 Jo, D. S., Hodzic, A., Emmons, L. K., Tilmes, S., Schwantes, R. H., Mills, M. J., Campuzano-Jost,
781 P., Hu, W., Zaveri, R. A., Easter, R. C., Singh, B., Lu, Z., Schulz, C., Schneider, J., Shilling,
782 J. E., Wisthaler, A., and Jimenez, J. L.: Future changes in isoprene-epoxydiol-derived
783 secondary organic aerosol (IEPOX SOA) under the Shared Socioeconomic Pathways: the
784 importance of physicochemical dependency, *Atmospheric Chemistry and Physics*, 21,
785 3395–3425, <https://doi.org/10.5194/acp-21-3395-2021>, 2021.
- 786 Jo, D. S., Tilmes, S., Emmons, L. K., Wang, S., and Vitt, F.: A new simplified parameterization
787 of secondary organic aerosol in the Community Earth System Model Version 2 (CESM2;



- 788 CAM6.3), Geoscientific Model Development, 16, 3893–3906,
789 <https://doi.org/10.5194/gmd-16-3893-2023>, 2023.
- 790 Kanakidou, M., Seinfeld, J. H., Pandis, S. N., Barnes, I., Dentener, F. J., Facchini, M. C., Van
791 Dingenen, R., Ervens, B., Nenes, A., Nielsen, C. J., Swietlicki, E., Putaud, J. P., Balkanski,
792 Y., Fuzzi, S., Horth, J., Moortgat, G. K., Winterhalter, R., Myhre, C. E. L., Tsigaridis, K.,
793 Vignati, E., Stephanou, E. G., and Wilson, J.: Organic aerosol and global climate
794 modelling: a review, Atmospheric Chemistry and Physics, 5, 1053–1123,
795 <https://doi.org/10.5194/acp-5-1053-2005>, 2005.
- 796 Kenagy, H. S., Heald, C. L., Tahsini, N., Goss, M. B., and Kroll, J. H.: Can we achieve atmospheric
797 chemical environments in the laboratory? An integrated model-measurement approach to
798 chamber SOA studies, Science Advances, 10, eado1482,
799 <https://doi.org/10.1126/sciadv.ado1482>, 2024.
- 800 Krapf, M., El Haddad, I., Bruns, E. A., Molteni, U., Daellenbach, K. R., Prévôt, A. S. H.,
801 Baltensperger, U., and Dommen, J.: Labile Peroxides in Secondary Organic Aerosol,
802 Chem, 1, 603–616, <https://doi.org/10.1016/j.chempr.2016.09.007>, 2016.
- 803 Kroll, J. H., Ng, N. L., Murphy, S. M., Flagan, R. C., and Seinfeld, J. H.: Secondary organic aerosol
804 formation from isoprene photooxidation under high-NO_x conditions: SOA FORMATION
805 FROM ISOPRENE OXIDATION, Geophys. Res. Lett., 32, n/a-n/a,
806 <https://doi.org/10.1029/2005GL023637>, 2005.
- 807 Kroll, J. H., Ng, N. L., Murphy, S. M., Flagan, R. C., and Seinfeld, J. H.: Secondary Organic
808 Aerosol Formation from Isoprene Photooxidation, Environ. Sci. Technol., 40, 1869–1877,
809 <https://doi.org/10.1021/es0524301>, 2006.



810 Lawrence, D. M., Fisher, R. A., Koven, C. D., Oleson, K. W., Swenson, S. C., Bonan, G., Collier,
811 N., Ghimire, B., Kampenhout, L. van, Kennedy, D., Kluzek, E., Lawrence, P. J., Li, F., Li,
812 H., Lombardozzi, D., Riley, W. J., Sacks, W. J., Shi, M., Vertenstein, M., Wieder, W. R.,
813 Xu, C., Ali, A. A., Badger, A. M., Bisht, G., Broeke, M. van den, Brunke, M. A., Burns, S.
814 P., Buzan, J., Clark, M., Craig, A., Dahlin, K., Drewniak, B., Fisher, J. B., Flanner, M.,
815 Fox, A. M., Gentine, P., Hoffman, F., Keppel-Aleks, G., Knox, R., Kumar, S., Lenaerts, J.,
816 Leung, L. R., Lipscomb, W. H., Lu, Y., Pandey, A., Pelletier, J. D., Perket, J., Randerson,
817 J. T., Ricciuto, D. M., Sanderson, B. M., Slater, A., Subin, Z. M., Tang, J., Thomas, R. Q.,
818 Martin, M. V., and Zeng, X.: The Community Land Model Version 5: Description of New
819 Features, Benchmarking, and Impact of Forcing Uncertainty, *Journal of Advances in*
820 *Modeling Earth Systems*, 11, 4245–4287, <https://doi.org/10.1029/2018MS001583>, 2019.

821 Liu, X., Easter, R. C., Ghan, S. J., Zaveri, R., Rasch, P., Shi, X., Lamarque, J.-F., Gettelman, A.,
822 Morrison, H., Vitt, F., Conley, A., Park, S., Neale, R., Hannay, C., Ekman, A. M. L., Hess,
823 P., Mahowald, N., Collins, W., Iacono, M. J., Bretherton, C. S., Flanner, M. G., and
824 Mitchell, D.: Toward a minimal representation of aerosols in climate models: description
825 and evaluation in the Community Atmosphere Model CAM5, *Geosci. Model Dev.*, 5, 709–
826 739, <https://doi.org/10.5194/gmd-5-709-2012>, 2012.

827 Liu, X., Ma, P.-L., Wang, H., Tilmes, S., Singh, B., Easter, R. C., Ghan, S. J., and Rasch, P. J.:
828 Description and evaluation of a new four-mode version of the Modal Aerosol Module
829 (MAM4) within version 5.3 of the Community Atmosphere Model, *Geosci. Model Dev.*,
830 9, 505–522, <https://doi.org/10.5194/gmd-9-505-2016>, 2016.

831 Lou, S., Shrivastava, M., Easter, R. C., Yang, Y., Ma, P.-L., Wang, H., Cubison, M. J.,
832 Campuzano-Jost, P., Jimenez, J. L., Zhang, Q., Rasch, P. J., Shilling, J. E., Zelenyuk, A.,



- 833 Dubey, M., Cameron-Smith, P., Martin, S. T., Schneider, J., and Schulz, C.: New SOA
834 Treatments Within the Energy Exascale Earth System Model (E3SM): Strong Production
835 and Sinks Govern Atmospheric SOA Distributions and Radiative Forcing, *Journal of*
836 *Advances in Modeling Earth Systems*, 12, e2020MS002266,
837 <https://doi.org/10.1029/2020MS002266>, 2020.
- 838 Mayhew, A. W., Franzon, L., Bates, K. H., Kurtén, T., Lopez-Hilfiker, F. D., Mohr, C., Rickard,
839 A. R., Thornton, J. A., and Haskins, J. D.: The global importance of gas-phase peroxy
840 radical accretion reactions for secondary organic aerosol loading, *Atmospheric Chemistry*
841 *and Physics*, 25, 17027–17046, <https://doi.org/10.5194/acp-25-17027-2025>, 2025.
- 842 Ng, N. L., Chhabra, P. S., Chan, A. W. H., Surratt, J. D., Kroll, J. H., Kwan, A. J., McCabe, D. C.,
843 Wennberg, P. O., Sorooshian, A., Murphy, S. M., Dalleska, N. F., Flagan, R. C., and
844 Seinfeld, J. H.: Effect of NO_x level on secondary organic aerosol (SOA) formation from
845 the photooxidation of terpenes, *Atmospheric Chemistry and Physics*, 7, 5159–5174,
846 <https://doi.org/10.5194/acp-7-5159-2007>, 2007.
- 847 O'Brien, R. E. and Kroll, J. H.: Photolytic Aging of Secondary Organic Aerosol: Evidence for a
848 Substantial Photo-Recalcitrant Fraction, *J. Phys. Chem. Lett.*, 10, 4003–4009,
849 <https://doi.org/10.1021/acs.jpcclett.9b01417>, 2019.
- 850 Otkjær, R. V., Jakobsen, H. H., Tram, C. M., and Kjaergaard, H. G.: Calculated Hydrogen Shift
851 Rate Constants in Substituted Alkyl Peroxy Radicals, *J. Phys. Chem. A*, 122, 8665–8673,
852 <https://doi.org/10.1021/acs.jpca.8b06223>, 2018.
- 853 Presto, A. A., Huff Hartz, K. E., and Donahue, N. M.: Secondary Organic Aerosol Production
854 from Terpene Ozonolysis. 2. Effect of NO_x Concentration, *Environ. Sci. Technol.*, 39,
855 7046–7054, <https://doi.org/10.1021/es050400s>, 2005.



- 856 Pye, H. O. T., Chan, A. W. H., Barkley, M. P., and Seinfeld, J. H.: Global modeling of organic
857 aerosol: the importance of reactive nitrogen (NO_x and NO₃), *Atmos. Chem. Phys.*, 10,
858 11261–11276, <https://doi.org/10.5194/acp-10-11261-2010>, 2010.
- 859 Pye, H. O. T., D’Ambro, E. L., Lee, B. H., Schobesberger, S., Takeuchi, M., Zhao, Y., Lopez-
860 Hilfiker, F., Liu, J., Shilling, J. E., Xing, J., Mathur, R., Middlebrook, A. M., Liao, J., Welti,
861 A., Graus, M., Warneke, C., de Gouw, J. A., Holloway, J. S., Ryerson, T. B., Pollack, I.
862 B., and Thornton, J. A.: Anthropogenic enhancements to production of highly oxygenated
863 molecules from autoxidation, *Proceedings of the National Academy of Sciences*, 116,
864 6641–6646, <https://doi.org/10.1073/pnas.1810774116>, 2019.
- 865 Riahi, K., van Vuuren, D. P., Kriegler, E., Edmonds, J., O’Neill, B. C., Fujimori, S., Bauer, N.,
866 Calvin, K., Dellink, R., Fricko, O., Lutz, W., Popp, A., Cuaresma, J. C., Kc, S., Leimbach,
867 M., Jiang, L., Kram, T., Rao, S., Emmerling, J., Ebi, K., Hasegawa, T., Havlik, P.,
868 Humpenöder, F., Da Silva, L. A., Smith, S., Stehfest, E., Bosetti, V., Eom, J., Gernaat, D.,
869 Masui, T., Rogelj, J., Strefler, J., Drouet, L., Krey, V., Luderer, G., Harmsen, M.,
870 Takahashi, K., Baumstark, L., Doelman, J. C., Kainuma, M., Klimont, Z., Marangoni, G.,
871 Lotze-Campen, H., Obersteiner, M., Tabeau, A., and Tavoni, M.: The Shared
872 Socioeconomic Pathways and their energy, land use, and greenhouse gas emissions
873 implications: An overview, *Global Environmental Change*, 42, 153–168,
874 <https://doi.org/10.1016/j.gloenvcha.2016.05.009>, 2017.
- 875 Schwantes, R. H., Emmons, L. K., Orlando, J. J., Barth, M. C., Tyndall, G. S., Hall, S. R., Ullmann,
876 K., St. Clair, J. M., Blake, D. R., Wisthaler, A., and Bui, T. P. V.: Comprehensive isoprene
877 and terpene gas-phase chemistry improves simulated surface ozone in the southeastern US,



- 878 Atmospheric Chemistry and Physics, 20, 3739–3776, <https://doi.org/10.5194/acp-20->
879 3739-2020, 2020.
- 880 Shi, Y., Heald, C. L., and Val Martin, M.: Future Anthropogenic Land Use Change Impacts on
881 Carbonaceous Aerosol and Implications for Climate and Air Quality, Geophysical
882 Research Letters, 52, e2024GL110962, <https://doi.org/10.1029/2024GL110962>, 2025.
- 883 Shi, Y., Heald, C. L., and Kroll, J. H.: Drivers of biogenic secondary organic aerosol from the past
884 to the future [data set], Zenodo, <https://doi.org/10.5281/zenodo.19038722>, 2026.
- 885 Song, C., Na, K., and Cocker, D. R.: Impact of the Hydrocarbon to NO_x Ratio on Secondary
886 Organic Aerosol Formation, Environ. Sci. Technol., 39, 3143–3149,
887 <https://doi.org/10.1021/es0493244>, 2005.
- 888 Sun, M. and Smith, G. D.: Photolytic Mass Loss of Humic Substances Measured with a Quartz
889 Crystal Microbalance, ACS Earth Space Chem.,
890 <https://doi.org/10.1021/acsearthspacechem.4c00134>, 2024.
- 891 Tilmes, S., Hodzic, A., Emmons, L. K., Mills, M. J., Gettelman, A., Kinnison, D. E., Park, M.,
892 Lamarque, J. -F., Vitt, F., Shrivastava, M., Campuzano-Jost, P., Jimenez, J. L., and Liu,
893 X.: Climate Forcing and Trends of Organic Aerosols in the Community Earth System
894 Model (CESM2), J. Adv. Model. Earth Syst., 11, 4323–4351,
895 <https://doi.org/10.1029/2019MS001827>, 2019.
- 896 Tsimpidi, A. P., Karydis, V. A., Pozzer, A., Pandis, S. N., and Lelieveld, J.: ORACLE (v1.0):
897 module to simulate the organic aerosol composition and evolution in the atmosphere,
898 Geoscientific Model Development, 7, 3153–3172, <https://doi.org/10.5194/gmd-7-3153->
899 2014, 2014.



- 900 Unger, N.: Human land-use-driven reduction of forest volatiles cools global climate, *Nature Clim*
901 *Change*, 4, 907–910, <https://doi.org/10.1038/nclimate2347>, 2014.
- 902 Vereecken, L. and Nozière, B.: H migration in peroxy radicals under atmospheric conditions,
903 *Atmos. Chem. Phys.*, 20, 7429–7458, <https://doi.org/10.5194/acp-20-7429-2020>, 2020.
- 904 Xu, L., Møller, K. H., Crounse, J. D., Otkjær, R. V., Kjaergaard, H. G., and Wennberg, P. O.:
905 Unimolecular Reactions of Peroxy Radicals Formed in the Oxidation of α -Pinene and β -
906 Pinene by Hydroxyl Radicals, *J. Phys. Chem. A*, 123, 1661–1674,
907 <https://doi.org/10.1021/acs.jpca.8b11726>, 2019.
- 908 Xu, R., Thornton, J. A., Lee, B. H., Zhang, Y., Jaeglé, L., Lopez-Hilfiker, F. D., Rantala, P., and
909 Petäjä, T.: Global simulations of monoterpene-derived peroxy radical fates and the
910 distributions of highly oxygenated organic molecules (HOMs) and accretion products,
911 *Atmospheric Chemistry and Physics*, 22, 5477–5494, [https://doi.org/10.5194/acp-22-](https://doi.org/10.5194/acp-22-5477-2022)
912 [5477-2022](https://doi.org/10.5194/acp-22-5477-2022), 2022.
- 913 Zawadowicz, M. A., Lee, B. H., Shrivastava, M., Zelenyuk, A., Zaveri, R. A., Flynn, C., Thornton,
914 J. A., and Shilling, J. E.: Photolysis Controls Atmospheric Budgets of Biogenic Secondary
915 Organic Aerosol, *Environ. Sci. Technol.*, 54, 3861–3870,
916 <https://doi.org/10.1021/acs.est.9b07051>, 2020.
- 917 Zhang, Q., Jimenez, J. L., Canagaratna, M. R., Allan, J. D., Coe, H., Ulbrich, I., Alfarra, M. R.,
918 Takami, A., Middlebrook, A. M., Sun, Y. L., Dzepina, K., Dunlea, E., Docherty, K.,
919 DeCarlo, P. F., Salcedo, D., Onasch, T., Jayne, J. T., Miyoshi, T., Shiono, A.,
920 Hatakeyama, S., Takegawa, N., Kondo, Y., Schneider, J., Drewnick, F., Borrmann, S.,
921 Weimer, S., Demerjian, K., Williams, P., Bower, K., Bahreini, R., Cottrell, L., Griffin, R.
922 J., Rautiainen, J., Sun, J. Y., Zhang, Y. M., and Worsnop, D. R.: Ubiquity and dominance



923 of oxygenated species in organic aerosols in anthropogenically-influenced Northern
924 Hemisphere midlatitudes, *Geophysical Research Letters*, 34,
925 <https://doi.org/10.1029/2007GL029979>, 2007.

926 Zhao, B., Shrivastava, M., Donahue, N. M., Gordon, H., Schervish, M., Shilling, J. E., Zaveri, R.
927 A., Wang, J., Andreae, M. O., Zhao, C., Gaudet, B., Liu, Y., Fan, J., and Fast, J. D.: High
928 concentration of ultrafine particles in the Amazon free troposphere produced by organic
929 new particle formation, *Proc. Natl. Acad. Sci.*, 117, 25344–25351,
930 <https://doi.org/10.1073/pnas.2006716117>, 2020.

931 Zhao, B., Donahue, N. M., Zhang, K., Mao, L., Shrivastava, M., Ma, P.-L., Shen, J., Wang, S.,
932 Sun, J., Gordon, H., Tang, S., Fast, J., Wang, M., Gao, Y., Yan, C., Singh, B., Li, Z., Huang,
933 L., Lou, S., Lin, G., Wang, H., Jiang, J., Ding, A., Nie, W., Qi, X., Chi, X., and Wang, L.:
934 Global variability in atmospheric new particle formation mechanisms, *Nature*, 631, 98–
935 105, <https://doi.org/10.1038/s41586-024-07547-1>, 2024.

936 Zhao, Y., Thornton, J. A., and Pye, H. O. T.: Quantitative constraints on autoxidation and dimer
937 formation from direct probing of monoterpene-derived peroxy radical chemistry,
938 *Proceedings of the National Academy of Sciences*, 115, 12142–12147,
939 <https://doi.org/10.1073/pnas.1812147115>, 2018.

940

941

942